The Journal of
Chemical Physics

RESEARCH ARTICLE | AUGUST 26 2025

A density functional theory study of thermally activated water splitting on the $CuWO_4$ (010) surface

Xuan Chu ; Nora H. de Leeuw

J. Chem. Phys. 163, 084712 (2025)
https://doi.org/10.1063/5.0283631

AIP
Publishing

The Journal
of Chemical Physics

ARTICLE

pubs.aip.org/aip/jcp

A density functional theory study of thermally activated water splitting on the $CuWO_4$ (010) surface

Cite as: J. Chem. Phys. **163**, 084712 (2025); doi: 10.1063/5.0283631
Submitted: 2 June 2025 • Accepted: 31 July 2025 •
Published Online: 26 August 2025

Xuan Chu[1,a)] and Nora H. de Leeuw[1,2,b)]

AFFILIATIONS

[1] School of Chemistry, University of Leeds, Leeds LS2 9JT, United Kingdom
[2] Department of Earth Sciences, Utrecht University, 3584CD Utrecht, The Netherlands

[a)] **Author to whom correspondence should be addressed:** cmxch@leeds.ac.uk
[b)] n.h.deleeuw@leeds.ac.uk

ABSTRACT

$CuWO_4$ shows promise as a suitable material for solar-driven water splitting to aid progress towards sustainable and carbon-free energy generation. In this work, we report a computational study of catalytic water splitting and hydrogen generation at $CuWO_4$ surfaces, employing calculations based on the density functional theory with on-site Coulomb and long-range dispersion corrections (DFT+U-D3). We have analyzed three potential thermodynamic and kinetic reaction profiles at the pristine $CuWO_4$ surface and one potential profile at the reduced $CuWO_4$ surface, examining the structural and electronic properties of the intermediates, as well as the transition states along the different pathways. Our findings reveal that along the pathway on the reduced surface, oxygen vacancies introduced in the surface led to under-coordinated Cu and W atoms and localized excess electrons, which significantly enhance the hydrogen evolution reaction.

I. INTRODUCTION

Photo-catalytic and photo-electrochemical water splitting at semiconductor surfaces offers a promising approach to directly convert solar energy into chemical energy in the form of hydrogen, a crucial component of a sustainable energy future.[1–6] The process begins with the absorption of photons, leading to the excitation of electrons into the conduction band and the generation of holes in the valence band. These photo-generated electrons and holes participate in the hydrogen evolution reaction (HER, $2H^+ + 2e^- \rightarrow H_2$) and oxygen evolution reaction (OER, $H_2O + h^+ \rightarrow 2H^+ + \frac{1}{2}O_2$), resulting in the production of hydrogen and oxygen from water.[7,8] To efficiently utilize the visible spectrum of sunlight, the bandgap of the semiconductor should ideally be around 2.0 eV.[9–11] Additionally, the bandgap must align with the redox potentials of water to enable both reduction and oxidation by the photo-generated charge carriers. Specifically, the conduction band minimum of the photo-catalyst should be more negative than 0 V (vs. the normal hydrogen electrode, NHE), while the valence band maximum should be more positive than 1.23 V (vs. NHE).[12] Consequently, the minimum bandgap required for water splitting is 1.23 eV, corresponding to a wavelength of ∼1000 nm.

Copper tungstate ($CuWO_4$) has emerged as a promising photo-catalyst and photo-electrocatalyst owing to its unique combination of structural, electronic, and chemical properties that could support efficient water splitting.[13–17] Its optimal bandgap of 2.3–2.4 eV allows it to absorb a significant portion of the visible spectrum, ensuring effective utilization of sunlight.[18] The conduction band edge of $CuWO_4$ is close to the hydrogen reduction potential, enabling efficient electron transfer for hydrogen production.[13] Moreover, its excellent chemical and photo-chemical stability in aqueous environments, particularly under oxidizing conditions, minimizes the risk of photo-corrosion, ensuring long-term functionality in water-splitting systems.[14] Significant research has been conducted to optimize the material through approaches such as doping,[15] creating heterojunctions,[19] and introducing oxygen vacancies.[20]

Recent experimental and theoretical studies have confirmed that introducing oxygen vacancies into the surface can substantially enhance the photocatalytic activity of $CuWO_4$.[21–23] Xiang *et al.* demonstrated that oxygen-deficient $CuWO_4$ exhibits significantly improved charge transfer and reduced activation barriers for water oxidation. Their DFT analysis showed that the first and second O–H bond-breaking steps are energetically more favorable on a reduced surface.[21] Similarly, Guo *et al.* reported that oxygen-vacancy-rich $CuWO_4/CuBi_2O_4$ heterostructures display superior visible-light-driven photocatalytic degradation due to enhanced interfacial charge separation.[22] Chen *et al.* showed that vacancy-engineered $CuWO_4$ nanoparticles possess increased charge carrier density, narrowed bandgaps, and higher surface reactivity, all of which contribute to superior photocatalytic performance.[23] These findings affirm that oxygen vacancies can tune the electronic structure and reactivity of $CuWO_4$, making defect engineering a promising route for improving water-splitting efficiency.

Our previous work has explored the structural, electronic, and redox properties of $CuWO_4$, as well as its interactions with water molecules.[24,25] However, the details of solar-driven water splitting at the $CuWO_4$ interface remain unclear. In this study, we have employed calculations based on the density functional theory (DFT) to first provide a detailed description of the mechanisms underlying the thermally activated water splitting process at the $CuWO_4$ surface. Three catalytic pathways applied over the pristine $CuWO_4$ (010) surface, as well as one pathway applied over the reduced $CuWO_4$ (010) surface, have been analyzed in terms of water adsorption, dissociation, hydrogen generation, and desorption. We have identified the thermodynamically and kinetically most favorable intermediates and transition states for each pathway, with a primary focus on their structures, charge density transfers, and the vibrational frequencies of the OH bond. Our findings offer valuable insights into the water splitting process at the $CuWO_4$ surface, thereby helping to accelerate viable hydrogen production pathways and advancing clean energy technologies.

II. METHODS

Here, we describe the computational setup used for the calculations and the creation of the surface model used to calculate the catalytic pathways.

A. DFT calculations

In this work, we have performed first-principles calculations at the spin-polarized density functional theory (DFT) level using the Vienna Ab initio Simulation Package (VASP).[26,27] The Perdew–Burke–Ernzerhof (PBE) functional was employed to compute the exchange–correlation term of the Kohn–Sham equation.[28] The projected augmented wave method was used to model the frozen core electrons, their kinetic energy densities, and their interactions with the valence states.[29] The 1s level of H, the 2s2p levels of O, the 3d4s levels of Cu, and the 5s5p5d6s levels of W were treated as valence states.

A periodic plane-wave basis set with a 400 eV cut-off energy was used to expand the Kohn–Sham valence states. To account for the van der Waals interactions, the Grimme D3 method with Becke–Johnson damping was applied.[30] To better simulate the bandgap of $CuWO_4$, we employed the DFT+U method to correct the electronic self-interaction in the d-orbitals of the transition metals, which is inadequately addressed by pure GGA functionals.[31] The on-site Coulomb term (U_{eff}) was tested in the range of 3–10 eV for both Cu and W cations. Our optimization provided the best agreement with experimental lattice parameters and band structures when U_{eff} was set to 7.5 eV for Cu. The results also indicated that the U correction is unnecessary for W atoms as they lose all their d-electrons upon the formation of $CuWO_4$. Although hybrid functionals offer an alternative to accurately describe the electronic properties of transition metals, they are highly system-dependent and require significantly more computational resources for surface models compared to the DFT+U method.[32,33] We have therefore adopted the DFT+U approach, whose accuracy in modeling $CuWO_4$ has been demonstrated in previous studies.[24,25]

Bulk $CuWO_4$, shown in Fig. 1(a), was modeled using a triclinic primitive unit cell containing 12 atoms ($Cu_2W_2O_8$), sampled with a Γ-centered 4 × 3 × 4 k-point mesh.[34] Isolated H_2, O_2, and H_2O

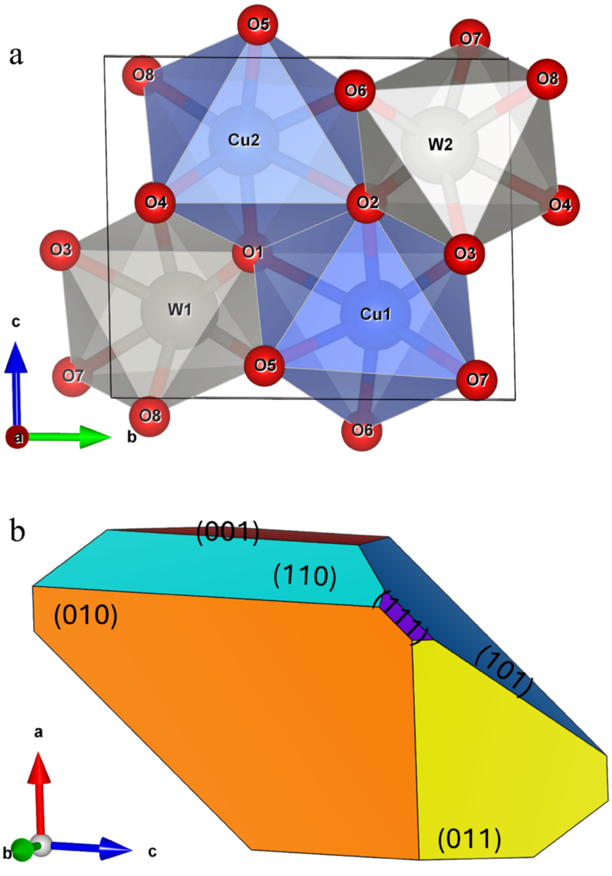

FIG. 1. (a) Polyhedral model of the triclinic $CuWO_4$ containing two formula units. Cu, W, and O are colored in blue, gray, and red, respectively. (b) Morphology of $CuWO_4$ under the conditions of water splitting (298 K).

molecules were sampled only at the Γ point in a 15 × 15 × 15 periodic simulation cell to avoid the influence of images in adjacent cells. The conjugate gradients algorithm was used to optimize the geometries of the bulk, dry surfaces, hydrated systems, and reaction intermediates. Optimization was deemed to be completed when the Hellmann–Feynman forces on each atom were less than 10^{-2} eV Å^{-1} and the energy difference between consecutive self-consistent steps was below 10^{-6} eV.[35] To increase the efficiency of the integration in the reciprocal space, we introduced the tetrahedron method with Blöchl correction for the bulk and surfaces of $CuWO_4$[36] and Gaussian smearing for the isolated H_2, O_2, and H_2O molecules.[37] We have also tested higher energy cutoffs and k-point grids, as well as lower self-consistent energy thresholds, to ensure that the energies were converged within 1 meV per atom.

The climbing image nudged elastic band (CI-NEB) method was applied to generate transition states along the catalytic pathways.[38,39] Five images were implied between the initial (IS) and the final state for the CI-NEB calculations.

The Bader charge of each atom was estimated by an improved grid-based algorithm proposed by Henkelman and co-workers.[40,41] This method uses zero flux surfaces to divide molecules into atoms, on which the charge density is the minimum perpendicular to the surface.

B. Surface model

The surface was created from the bulk $CuWO_4$ material according to the Tasker method[42] using the METADISE package,[43] and the calculations were carried out on a non-dipolar and symmetrical stoichiometric slab with Miller index (010). The surface slab was composed of 16 formula units of $CuWO_4$ in eight cation-oxygen mixed layers, where the four top-most layers were allowed to relax explicitly, while the atoms in the four layers at the bottom of the slab were kept fixed at their bulk-optimized positions. The exposed area of the surface was 91.85 Å^2, and a 10 Å vacuum was introduced perpendicular to the slab to prevent the interaction between the periodically repeated images of the $CuWO_4$ slab and to allow space to adsorb the H_2O molecules and follow the surface reactions. The surface energy of the slab before and after relaxation is calculated as

$$\gamma_u = \frac{E_u - nE_b}{2A}, \tag{1}$$

$$\gamma_r = \frac{E_r - nE_b}{A} - \gamma_u, \tag{2}$$

where E_r and E_u are the energies of the relaxed and unrelaxed slabs, respectively, and E_b is the energy of one formula unit of the bulk material. A represents the area of the slab, and n is the number of formula units in the slab.

C. Vibrational frequency calculations

We calculated the vibrational frequencies for the isolated H_2O molecule and the reaction intermediates for each step in the mechanistic pathways. The finite difference approach was applied, and the harmonic vibrational frequency was generated based on the second derivative of the potential energy with respect to the atomic position in the vicinity of the minimum of the well. A displacement of 0.015 Å was set for each ion to calculate the Hessian matrix. To compare with the experimental results, which were estimated between $v = 0$ and $v = 1$ vibrational energy levels of an anharmonic potential energy surface, a correction was introduced to the harmonic vibrational frequency through a scaling factor, which is defined as follows:[44–47]

TABLE I. Bond distance (d), bond angle (∠), stretching mode for H_2 (ν), asymmetrical stretching mode (ν_a), symmetrical stretching mode (ν_s), as well as bending mode (δ) for H_2O.

	H_2			H_2O	
Properties	Calculation	Experiment		Calculation	Experiment
d (Å)	0.74	0.75[48]		0.97	0.96[50]
∠	⋯	⋯		104.4°	104.5°[50]
ν(cm^{-1})	4315	4401[49]	ν_a(cm^{-1})	3683	3756[51]
			ν_s(cm^{-1})	3642	3657[51]
			δ(cm^{-1})	1522	1595[52]

$$\lambda = \sum_{i=1}^{all} \omega_i^{theor} \nu_i^{exp} \Big/ \sum_{i=1}^{all} \left(\omega_i^{theor}\right)^2, \tag{3}$$

where ω_i^{theor} and ν_i^{exp} are the ith calculated harmonic vibrational frequency and experimental fundamental frequency (in cm^{-1}), respectively.

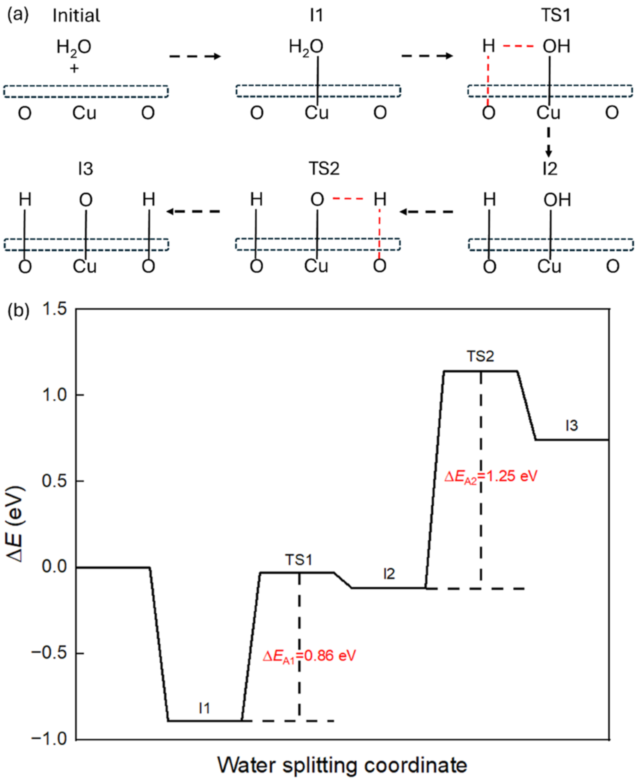

FIG. 2. (a) Proposed mechanism and (b) calculated reaction profile of pathway 1 on the $CuWO_4$ (010) surface.

D. Thermodynamic and kinetic profiles

The energy (ΔE_i) of the intermediates and the transition states along the thermodynamic and kinetic profiles with respect to the energy of the pristine (010) surface (E_{slab}) were calculated according to the following equation:

$$\Delta E_i = E_{\text{system}} - nE_{H_2O} - E_{\text{slab}} + lE_{H_2} + mE_{O_2}, \tag{4}$$

where E_{system} is the energy of the system with adsorbates; E_{H_2O}, E_{H_2}, and E_{O_2} are the energies of the isolated H_2O, H_2, and O_2 molecules in vacuum, respectively; n represents the number of adsorbed H_2O; and l and m are the number of H_2 and O_2 released from the surface system, respectively.

The activation energy (E_{Aj}) is calculated from the energy difference of the transition state i (ΔE_i) and intermediate $i-1$ (ΔE_{i-1}). It is worth noting that we have omitted the zero-point energy and vibrational contribution to the entropy since they have a negligible impact on the results, as tested in previous work.[24]

III. RESULTS AND DISCUSSION

A. Isolated molecules

The isolated hydrogen and water molecules in the gas phase were simulated in a 15 × 15 × 15 simulation cell to avoid the influence of the adjacent cells, where only the Γ point was sampled. The structural and electronic properties of bond distances, bond angles,

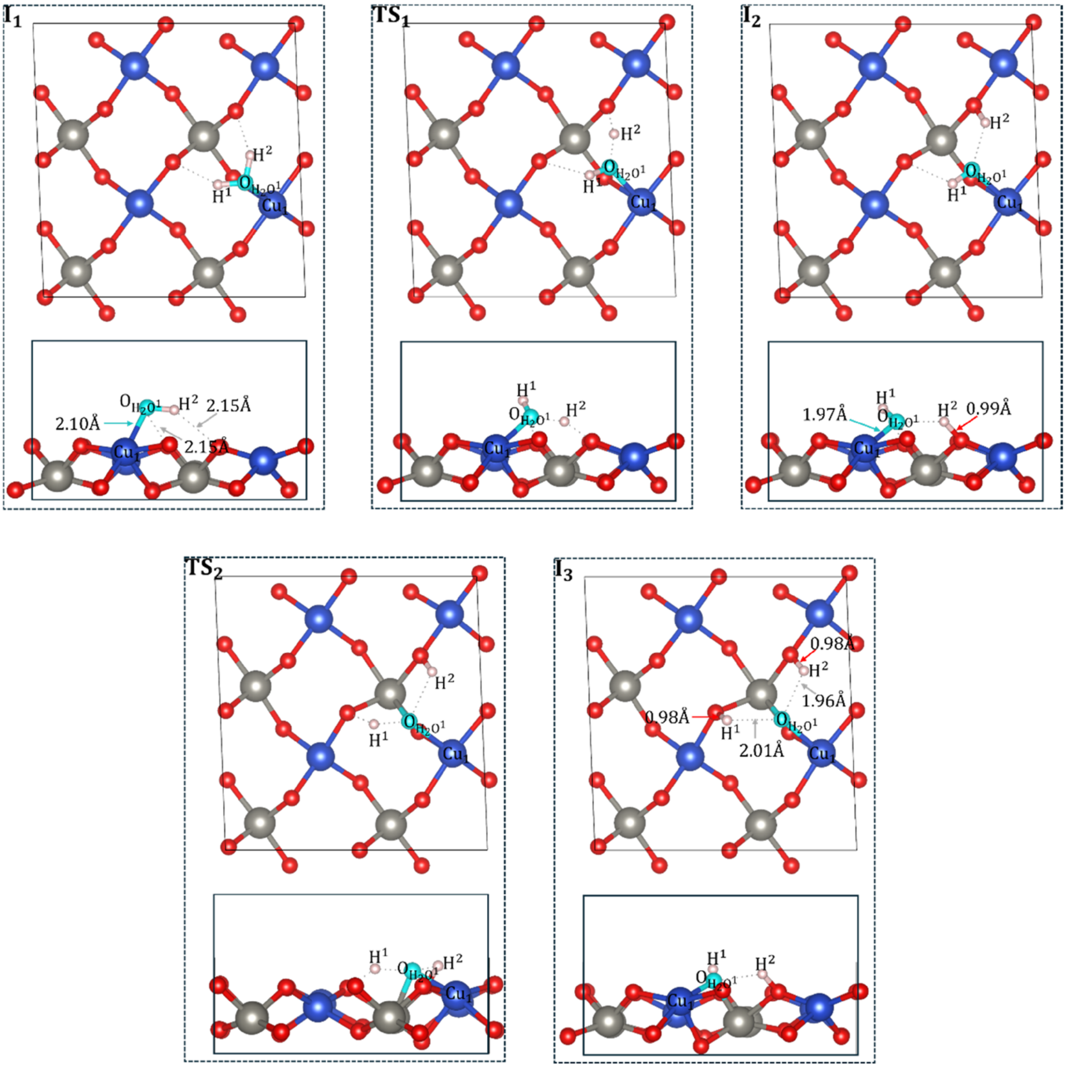

FIG. 3. Top and side views of the structures of the intermediates and transition states along pathway 1 on the pristine $CuWO_4$ (010) surface. The Cu, W, and O atoms of the surface are shown in blue, gray, and red, respectively. The O and H atoms of the water molecule are shown in cyan and white, respectively, and hydrogen-bonds are shown as dotted lines.

and harmonic vibrational frequencies of both hydrogen and water are listed in Table I. Our calculated equilibrium bond distances and bond angles for H_2 and H_2O are in good agreement with experiment. The simulated vibrational frequency of H_2 and the H_2O red shift are within 100 cm^{-1} of the experimental values, with the discrepancies due to the underestimation of the second derivative of energy with respect to atomic displacement by the PBE functional.

B. Pathways on the pristine $CuWO_4$ (010) surface

In previous work, we have investigated the redox properties of the low Miller index surfaces of $CuWO_4$, where the surface phase diagrams were reported as a function of partial pressure of oxygenated species and temperature.[25] The equilibrium crystal morphology of $CuWO_4$, derived from the phase diagrams under the conditions of mixtures of H_2O/H_2, suggests that the pristine (010) surface is the predominant facet in the morphology at 298 K [see Fig. 1(b)].[25] Further analysis of water adsorption confirmed that a H_2O molecule can adsorb onto the perfect (010) surface with an exothermic adsorption energy of −0.89 eV. Additionally, the bandgap at each coverage of H_2O on $CuWO_4$ remains greater than 1.23 eV, thus satisfying the minimum requirement of the bandgap for the water splitting reaction.[24] Consequently, in this work, we have selected the (010) surface for the mechanistic study of the water splitting reaction catalyzed by $CuWO_4$.

1. Pathway 1

The reaction profile of proposed mechanism 1 for the onset of water splitting is shown in Fig. 2. Only one water molecule is involved in this mechanism, corresponding to a surface coverage of 0.125 monolayers (ML). It is worth noting that in previous work, we had defined a full ML as eight H_2O molecules hydrating all four Cu atoms in the top-most layer of the surface.[24] A water molecule (H_2O^1) was first adsorbed on Cu^1 in the top-most layer at 2.03 Å, generating four non-equivalent types of Cu ions, as shown in state intermediate 1 (I1) of Fig. 3. Two hydrogen bonds were formed between H^1 and H^2 and the O atoms in the surface ($O_{surface}$) at distances of 2.15 and 2.21 Å, respectively. The process is exothermic with ΔE_1 calculated at −0.89 eV with respect to the pristine surface (reference system). The charge analysis of I1 indicates that an overall charge of 0.10 e^- was transferred from the adsorbate to the surface, mainly distributed along the $Cu_1O_{H_2O^1}$ bond, as shown in Fig. 4. The asymmetrical (υ_{as}) and symmetrical stretching modes (υ_s) of the water underwent a red shift after adsorption with respect to the isolated molecule in the gas phase (see Fig. 5), suggesting weakening of the OH bond, which is consistent with the charge migration from the adsorbate to the surface.

The next step is the dissociation of the adsorbed water molecule, which is an endothermic process with an ΔE_2 of 0.77 eV and an activation energy E_{A1} of 0.86 eV, as shown in stage I2 in Fig. 2. As shown in Fig. 5, a stretching mode (υ) of the $O_{H_2O^1}H_2$ group has disappeared, whereas a stretching mode of an $O_{surface}$ H_2 group was observed at 3260 cm^{-1}, supporting the dissociation of the water molecule. The vibrational stretching mode of the $O_{H_2O^1}H^1$ group exhibited a blue shift compared to the previous adsorption step, indicating a strengthening of the O–H bond after complete dissociation. The $O_{H_2O^1}H^1$ group is coordinated to Cu_1 at a distance of 1.97 Å, whereas the dissociated H^2 atom is bound to the surface at 0.99 Å (see Fig. 3). More charge has migrated to the surface with respect to the previous stage. As shown in Fig. 4, a total charge density of 0.47 e^- has been transferred from the adsorbate to the surface, mainly located along the $Cu_1O_{H_2O^1}$ and $O_{surface}H^2$ bonds. A charge density of 0.52 e^- was gained by the surface, mostly contributed by H^2 due to the dissociation of the water molecule, resulting in a more chemically reactive surface.

The following step involves the dissociation of the $O_{H_2O^1}H^1$ group. Formation of I3 is again an endothermic process with an activation energy E_{A2} of 1.25 eV and a reaction energy ΔE_3 of 0.85 eV (see Fig. 2). The stretching mode of $O_{H_2O^1}H^1$ has disappeared, but an $O_{surface}H^1$ stretching mode has appeared at 3518 cm^{-1}, Fig. 5, supporting the dissociation of the $O_{H_2O^1}H^1$ group. The stretching mode of $O_{H_2O^1}H^1$ exhibited a red shift with respect to the previous step, suggesting a weaker O–H bond after dissociation. However, the stretching mode of the $O_{surface}H^2$ group is blue-shifted by 197 cm^{-1} with respect to the previous step, indicating a strengthened OH

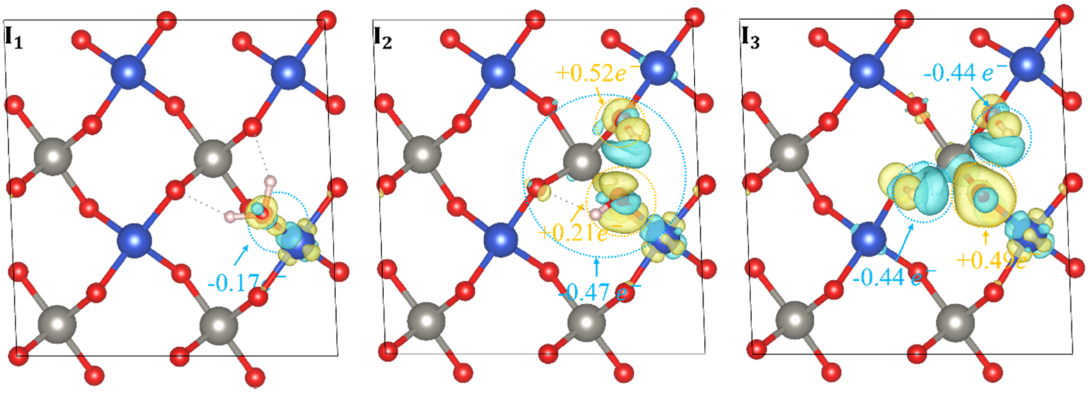

FIG. 4. Charge density differences for each stage of the water splitting process along pathway 1 on the $CuWO_4$ (010) surface. The blue regions represent charge gain, whereas the yellow regions represent charge depletion.

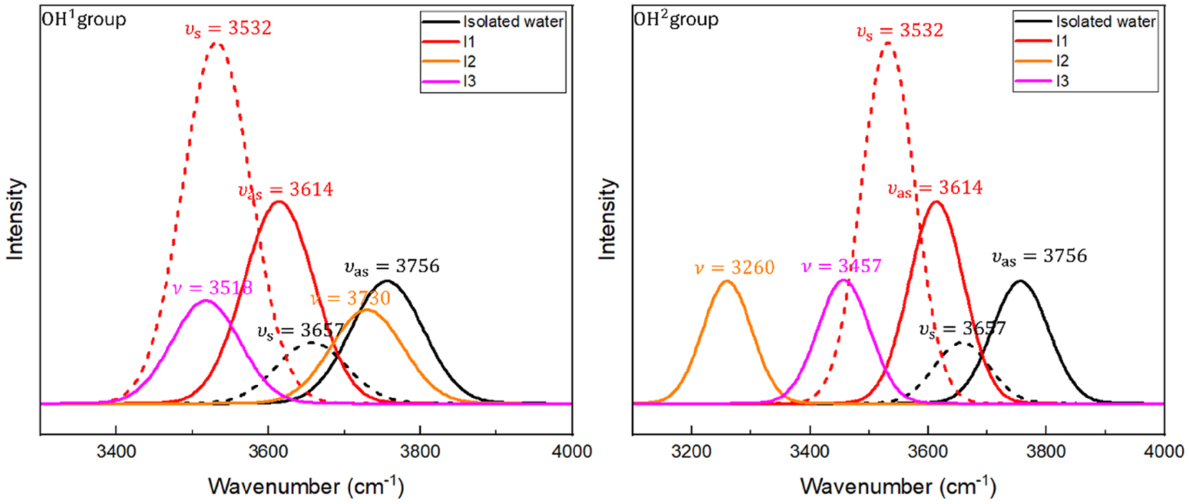

FIG. 5. Simulated IR spectra of the OH^1 (left panel) and OH^2 (right panel) bonds along the water splitting pathway 1 on the (010) surface. The spectra of isolated gas phase water and I1, I2, and I3 are colored in black, red, orange, and pink, respectively. υ are the stretching modes of the OH group for each intermediate, which are noted in the figure. υ_{as} and υ_s represent the asymmetrical and symmetrical stretching modes of molecular water, respectively.

bond. As shown in Fig. 3, the H^1 atom is bound to $O_{surface}$ at a distance of 0.98 Å, forming a hydrogen-bond with $O_{H_2O^1}$ at 2.01 Å. The H^2 atom binds to $O_{surface}$ at a distance of 0.98 Å, forming a hydrogen-bond with $O_{H_2O^1}$ at 1.96 Å. A total charge of 0.40 e^- is transferred from the water to the surface, mainly localized along the $Cu_1O_{H_2O^1}$, $W_1O_{H_2O^1}$, and $O_{surface}$ H bonds, as shown in Fig. 4. The H^1 and H^2 atoms have contributed a charge density of 0.88 e^- when bonding to $O_{surface}$, whereas $O_{H_2O^1}$ gained 0.49 e^- from coordination to the Cu_1 and W_1 atoms. Less charge was lost by the H^2 atom with respect to the previous step, which is consistent with the blue shift of the stretching mode of the $O_{surface}H^2$ group and increased bond strength.

Further steps involved the formation and desorption of H_2 and O_2, which requires energy to overcome activation barriers as well as the binding energy that keeps them attached to the surface. A reaction energy ΔE_4 of 4.59 eV with respect to the previous step indicates that the formation and desorption of one H_2 molecule from this surface at low water coverage is not thermodynamically feasible.

2. Pathway 2

In pathway 1, we found that the bond strength of the $O_{surface}H$ group weakens at stages I1, I2, and I3 due to more charge density migrating to the surface after adsorption and dissociation. Increasing the surface coverage of water stabilizes the intermediates and facilitates the formation and desorption of hydrogen molecules.

In pathway 2, as shown in Fig. 6, an additional water molecule was introduced to the system after stage I3 of pathway 1, corresponding to a surface coverage of 0.25 ML. A reaction energy of 0.12 eV with respect to the reference system of the pristine surface was observed at stage I4, which is 0.62 eV lower than stage I3,

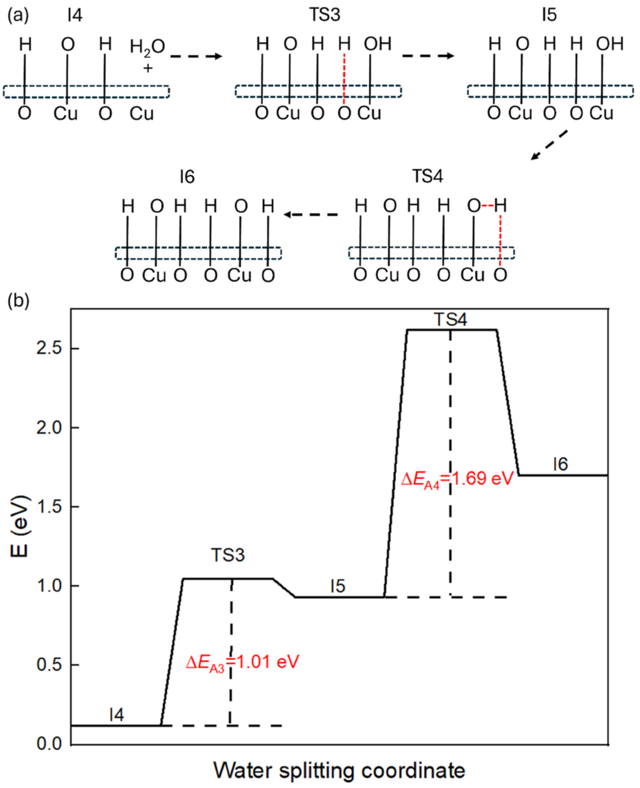

FIG. 6. (a) Proposed mechanism and (b) calculated reaction profile of pathway 2 on the $CuWO_4$ (010) surface.

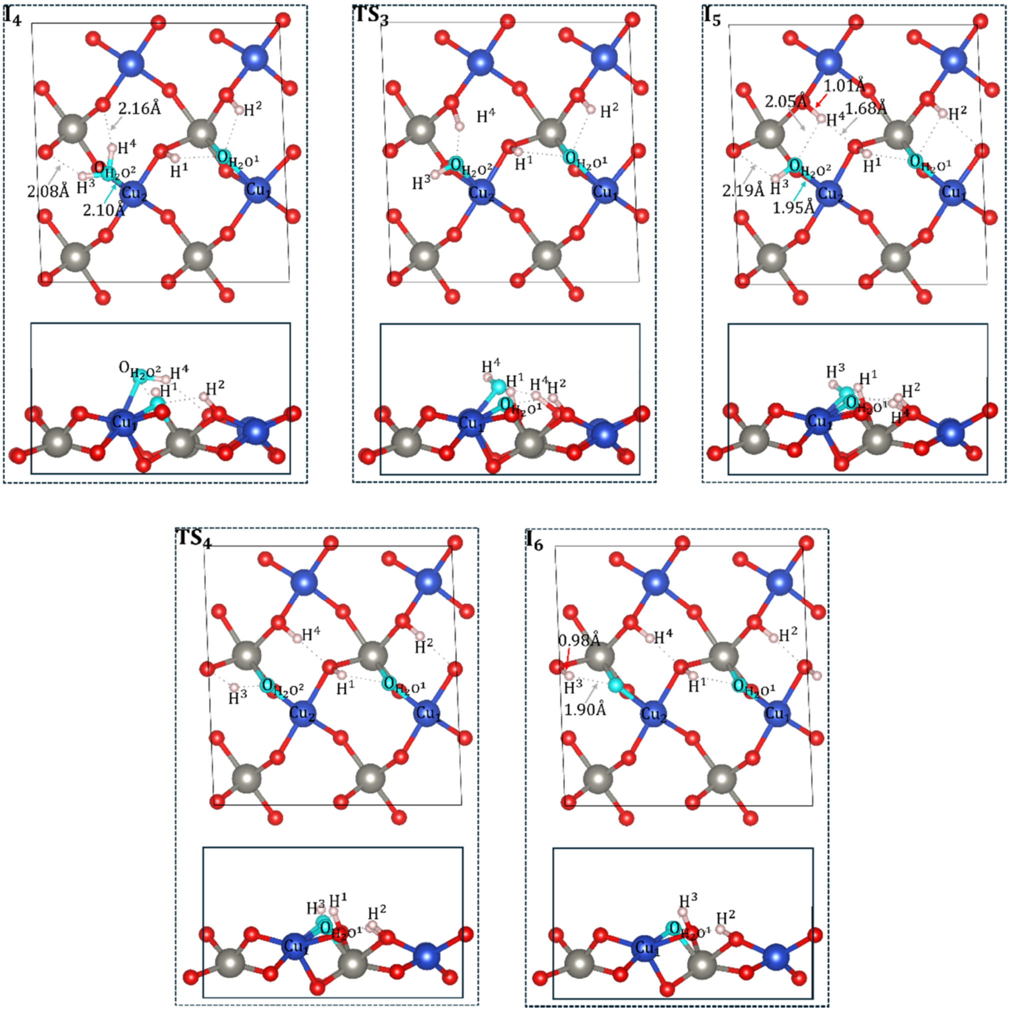

FIG. 7. Top and side views of the structures of the intermediates and transition states along pathway 2 on the $CuWO_4$ (010) surface. The Cu, W, and O atoms on the surface are in blue, gray, and red, respectively. The O and H atoms of the water are in cyan and white, respectively, and hydrogen-bonds are shown as dotted lines.

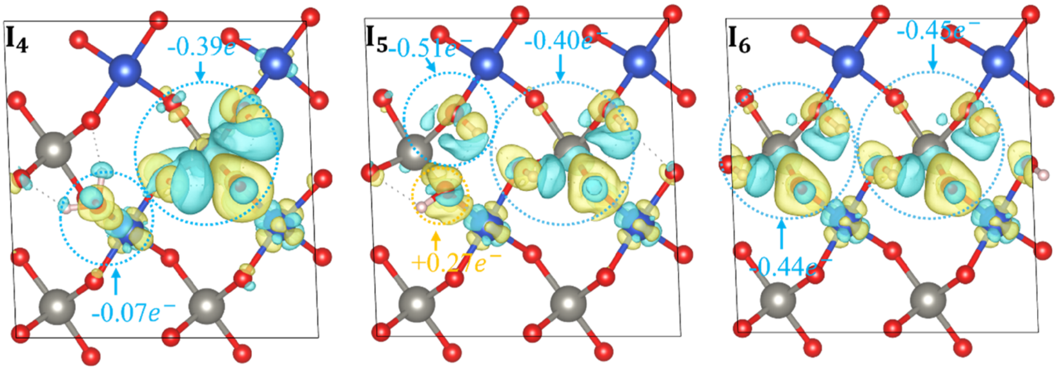

FIG. 8. Charge density difference plots of the different stages along pathway 2 of the water adsorption process on $CuWO_4$ (010) surface 2. Blue regions represent charge gain, whereas yellow regions represent charge depletion.

indicating that the adsorption of a second water molecule is exothermic. As shown in Fig. 7, the second adsorbed water (H_2O^2) located on Cu_2 at 2.10 Å formed hydrogen-bonds with $O_{surface}$ at 2.08 Å and 2.16. A total amount of 0.46 e^- migrated from the adsorbates to the surface, mostly distributed along the Cu-O_{H_2O} and $O_{surface}$-H bonds (see Fig. 8). $O_{H_2O^1}$ lost 0.39 e^- to the surface, i.e., only 0.02 e^- less compared to the previous step I3. However, an additional charge density of 0.07 e^- migrated from the $O_{H_2O^2}$ to the surface, resulting in the system becoming chemically more reactive. The symmetrical and asymmetrical stretching modes of the adsorbed water molecule were calculated at 3601.5 and 3523.2 cm^{-1}, respectively, as shown in Fig. 9, which exhibited a red shift with respect to the isolated water molecule, indicating weaker OH bonds. The stretching modes of OH^1 and OH^2 are red shifted to 3417 and 3425 cm^{-1}, respectively, compared to the previous step, because the adsorption of the additional water molecule caused more charge to be lost by the H atoms to the surface.

The next step to I5 involved the dissociation of $O_{H_2O^2}$, with an endothermic energy ΔE_5 of 0.81 eV with respect to the previous step with an activation energy E_{A3} of 1.01 eV (see Fig. 6). A stretching vibrational mode of 2994 cm^{-1} of the $O_{surface}$ H_4 group supports the dissociation of the water molecule (see Fig. 9). Compared to I4, the stretching mode of the $O_{surface}$ H_4 group is red-shifted, indicating weakening of the OH bond. The stretching mode of the $O_{H_2O2}H^3$ group was calculated at 3737 cm^{-1}, which is blue-shifted with respect to the previous stage (molecular water), indicating that the OH^3 bond was strengthened after dissociation, whereas blue shifts of the stretching modes of OH^1 and OH^2 were negligible compared to

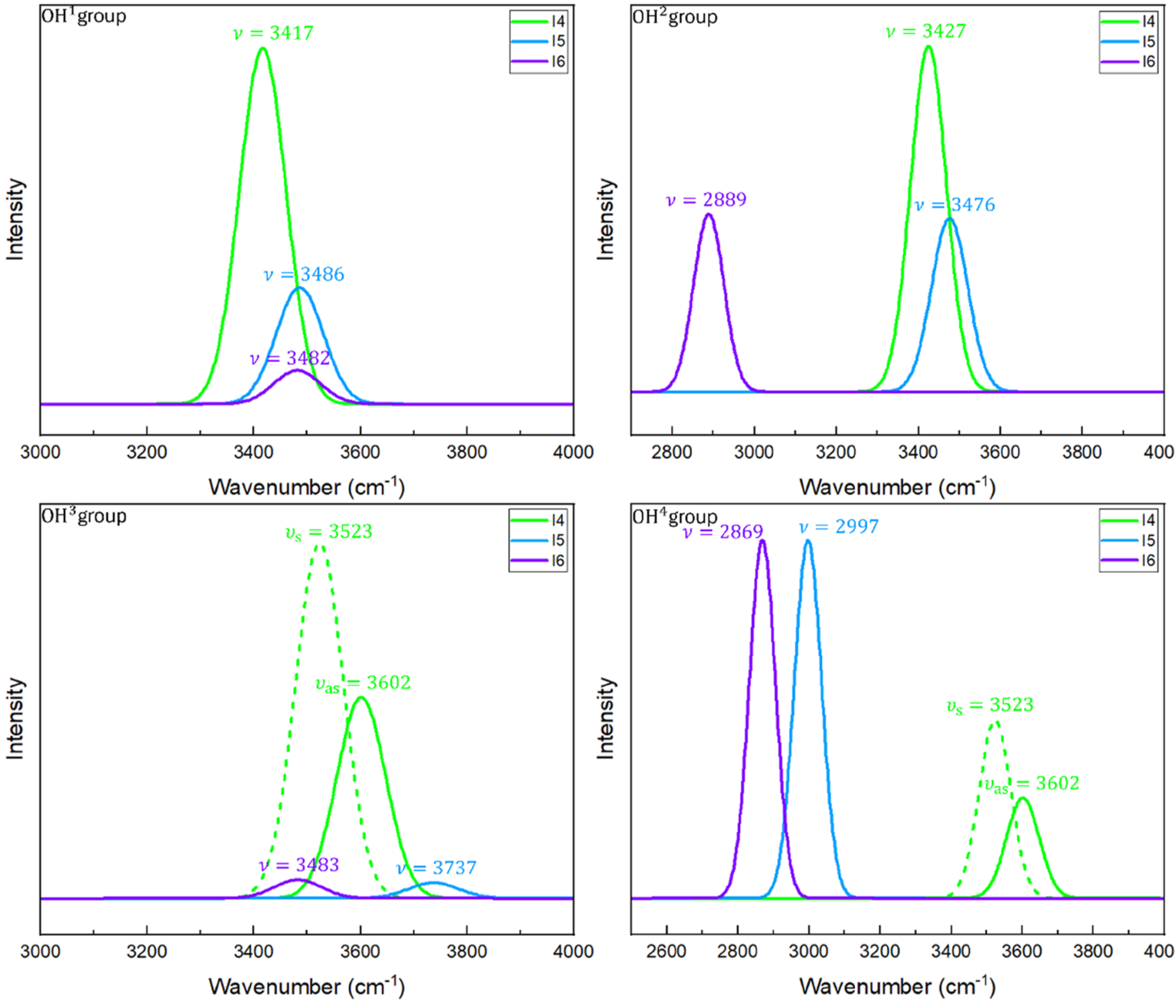

FIG. 9. Simulated IR spectra of OH^1 (left top panel), OH^2 (right top panel), OH^3 (left bottom panel), and OH^4 (right bottom panel) groups of pathway 2 on the (010) surface. The spectra of I4, I5, and I6 are colored in green, blue, and purple, respectively. υ is the stretching mode of the OH group for each intermediate, which is noted in the figure. ν_{as} and ν_s represent the asymmetrical and symmetrical stretching modes of molecular water, respectively.

stage I4. As shown in Fig. 7, the H^4 hydrogen bound to the surface at 1.01 Å forms hydrogen-bonds with O_{H_2O2} at 2.05 Å and with $O_{surface}$ at 1.68 Å. The $O_{H_2O^2}H^3$ group situated over Cu_2 at a distance of 1.95 Å forms a hydrogen-bond with $O_{surface}$ at 2.19 Å. The charge analysis indicates that a charge of 0.64 e^- was transferred from the adsorbates to the surface, contributing to the formation of CuO_{H_2O} bonds, a WO_{H_2O} bond, and $O_{surface}H$ bonds (see Fig. 8). $O_{H_2O^1}$ lost 0.40 e^- to the surface, which is identical to the previous step. An extra charge density of 0.24 e^- was lost by $O_{H_2O^2}$, thereby mainly contributing to the dissociation of the water molecule. The $O_{H_2O^2}H^3$ group gained 0.27 e^-, resulting in the blue shift of the stretching vibrational mode and a stronger OH bond, whereas H^4 contributed 0.51 e^- to the surface, which is consistent with the red shift of the stretching mode of the OH^4 group and weakening of the OH bond.

The $O_{H_2O^2}H^3$ group became dissociated at stage I6 (see Fig. 6), with a positive reaction energy of ΔE_6 of 0.77 eV with respect to the previous step and an activation energy E_{A3} of 1.69 eV, indicating that the step to form I6 is endothermic. As shown in Fig. 9, we obtained a stretching mode of the $O_{surface}H^3$ group at 3483 cm^{-1}, whereas the stretching mode of the $O_{H_2O^2}H^3$ group vanished, supporting the dissociation of the OH group. The stretching modes of OH^2 and OH^4 exhibited a red shift with respect to the previous stage I5, indicating weakening of the OH bonds. The structure of the intermediate I6 system is shown in Fig. 7. The proton H^3 is bound to the surface at a distance of 0.98 Å, and a hydrogen-bond was formed between H^3 and $O_{H_2O^2}$ at 1.90 Å, whereas the rest of the atoms stayed in the same positions as in the previous stage. Charge analysis indicates that a charge density of 0.89 e^- was transferred from the adsorbates to the surface (see Fig. 8). Specifically, $O_{H_2O^1}$ contributed 0.45 e^- to the surface, whereas $O_{H_2O^2}$ lost 0.44 e^- to the surface. The extra charge density transferred to the surface with respect to the previous stage I5 came mainly from the H^2, H^3, and H^4 atoms, which is consistent with the red shift of the stretching modes of the OH bonds.

We evaluated the generation of a hydrogen molecule using H^1 and H^3, as well as H^2 and H^4, based on the I6 structure, but the calculated energies ΔE_7 with respect to the previous step to generate such a single hydrogen molecule were 3.63 and 3.66 eV, respectively. These results indicate that hydrogen gas generation via pathway 2 is both kinetically and thermodynamically unfavorable. However, it is more favorable than pathway 1 as the greater charge transfer from the adsorbates to the surface weakens the OH bonds and enhances the chemical reactivity of the surface.

We also examined water splitting and hydrogen generation under conditions of higher surface coverage by water. In this case, the activation energy for the dissociation of the OH group increased due to the occupation of more surface sites, which impeded the water splitting. Therefore, an alternative mechanism involving greater charge density migration is required to lower the energy of the intermediates and the activation energies for hydrogen generation.

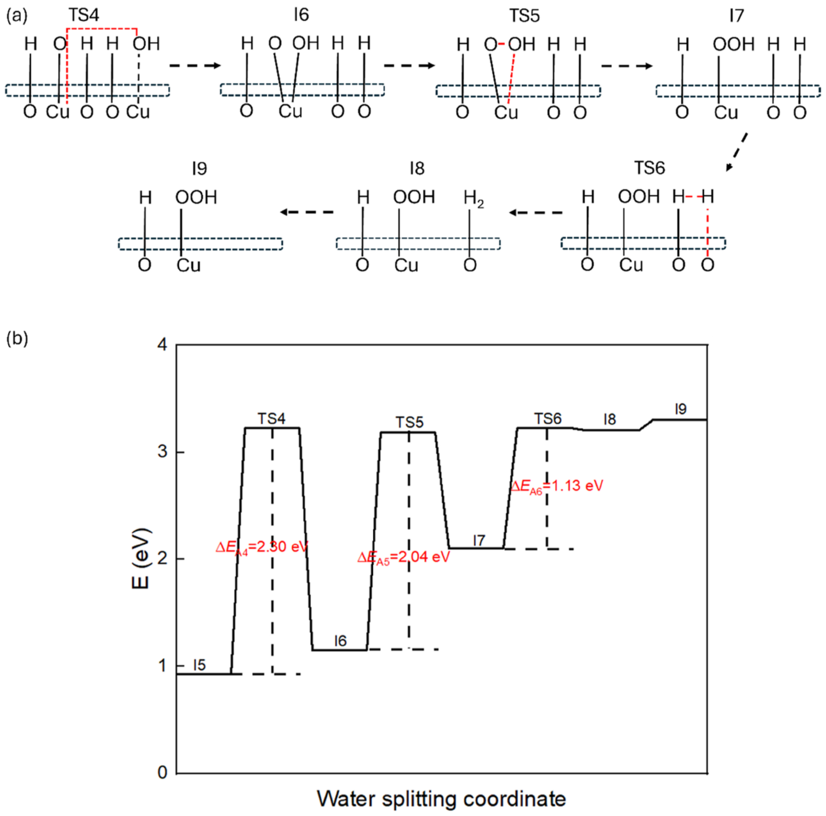

FIG. 10. (a) Proposed mechanism and (b) calculated reaction profile of pathway 3 on the $CuWO_4$ (010) surface.

3. Pathway 3

Inspired by work that mentions the formation of a hydroperoxyl group in the water splitting reaction,[52] we have calculated the formation of an $*$OOH group via pathway 3, where the first five intermediates of pathway 3 are identical to pathway 2.

At stage I6, the $O_{H_2O^2}H^3$ group migrated from Cu_2 to Cu_1 with a ΔE_6 of 0.77 eV with respect to the reference system and an activation energy E_{A4} of 2.30 eV, as shown in Fig. 10. A stretching mode of 958 cm^{-1} and a bending mode of 485 cm^{-1} for the $Cu_1O_{H_2O^2}$ group, together with the vanishing of the stretching mode, support the migration of the hydroxyl group. Further focusing on the stretching mode of the OH group of I6 (see Fig. 13), we note negligible changes in the stretching modes of the OH^1, OH^2, and OH^3 groups with respect to stage I5. However, the stretching mode of OH^4 exhibited a red shift by 882 cm^{-1} compared to stage I5, indicating weakening of the OH bond. The structure of I6 is shown in Fig. 11 with the $O_{H_2O^2}H^3$ group binding to Cu_1 at a distance of 1.91 Å. The $Cu_1O_{H_2O^2}$ bond lengthened to 2.59 Å due to the Coulomb attraction of $O_{H_2O^2}$, whereas the rest of the atoms stayed at the same position as in stage I5. Charge analysis shows that 0.68 e^- was transferred from the water molecules to the surface, mostly located along the $Cu_1O_{H_2O^1}$ bond, $Cu_1O_{H_2O^2}$ bond, $WO_{H_2O^1}$ bond, and $O_{surface}$ H bonds, as shown in Fig. 12. H_2O^1 contributed 0.51 e^- to the surface, whereas H_2O^2 lost 0.17 e^-. We found that $O_{H_2O^2}$ gained 0.22 e^-, mostly from Cu_1 and W, whereas hardly any charge was lost from the H^1, H^2, and H^3 atoms to the surface compared to stage I5, which is consistent with the negligible differences in the stretching modes. However, an extra charge density of 0.11 e^- was transferred from H^4 to the surface, which agrees with the red shift of the stretching mode and a weaker OH^4 bond.

The next step involved the formation of a hydroperoxyl group (see stage I7 in Fig. 10), with a reaction energy ΔE_7 of 0.95 eV and

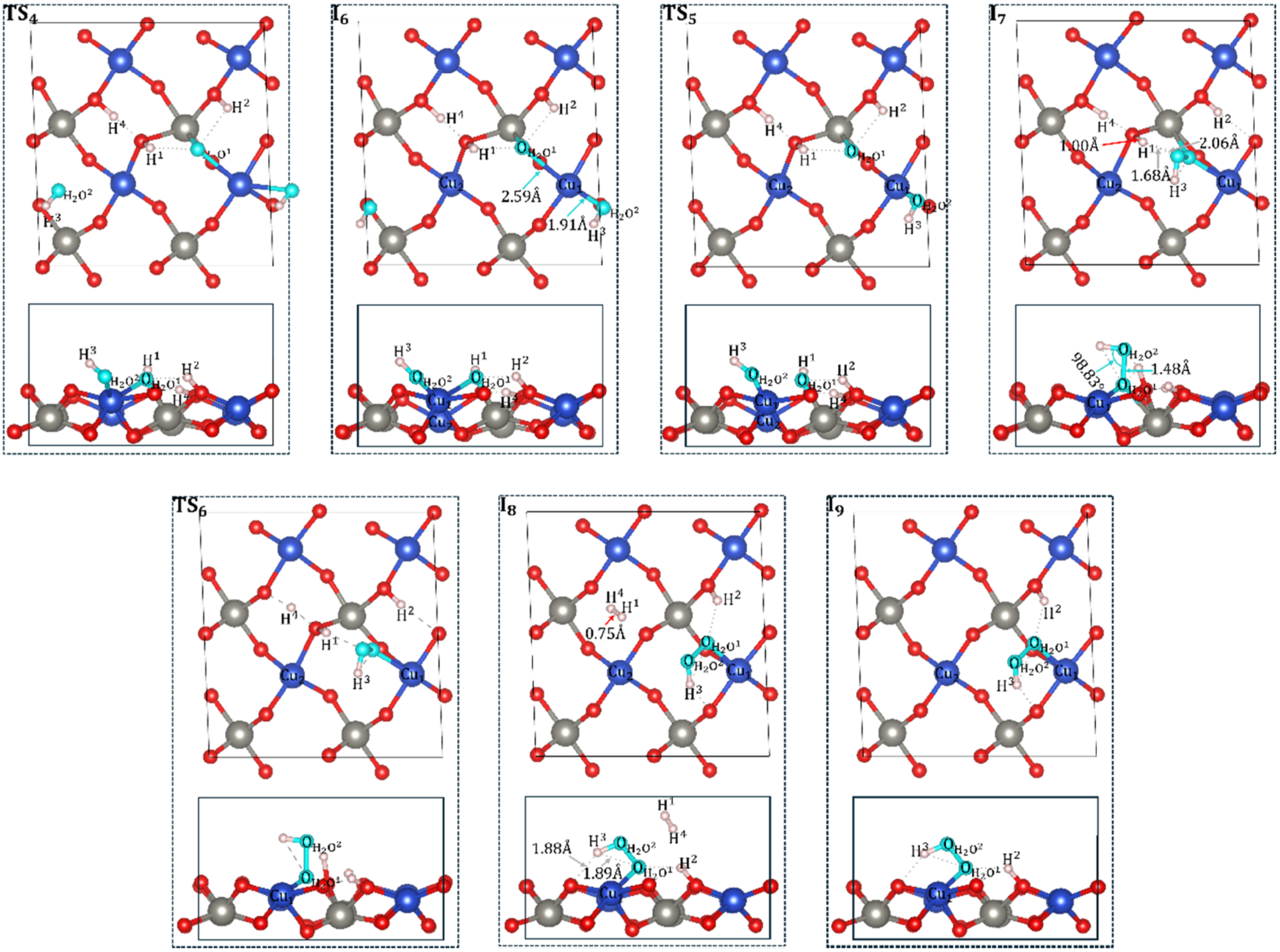

FIG. 11. Top and side view of the structures of the intermediates and transition states along pathway 3 on the $CuWO_4$ (010) surface. The Cu, W, and O atoms on the surface are in blue, gray, and red, respectively. The O and H atoms of the water are in cyan and white, respectively, and hydrogen-bonds are shown as dotted lines.

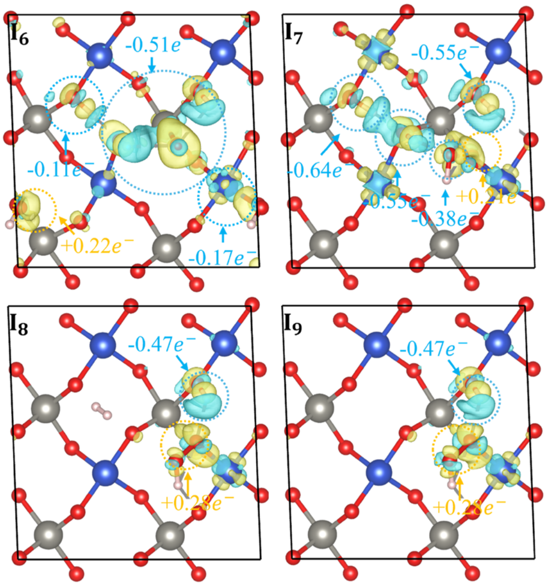

FIG. 12. Charge density difference plots for the different stages along the water splitting process via pathway 3 on the $CuWO_4$ (010) surface. Blue regions represent charge gain, whereas yellow regions represent charge depletion.

an activation energy E_{A5} of 2.04 eV from the previous step. We calculated the stretching mode of the $O_{H_2O^1}O_{H_2O^2}$ group at 845 cm^{-1}, shown in Fig. 14, supporting the formation of a hydroperoxyl group. Further vibrational information shows a red shift of the stretching modes of the OH^1, OH^2, and OH^3 groups with respect to the previous stage, indicating weakening of the OH bonds. The stretching mode of the OH^4 group changed only negligibly compared to I6. The $O_{H_2O^2}H^3$ group was located on top of $O_{H_2O^1}$ at 1.48 Å, forming the OOH group (see Fig. 11). The angle ∠OOH was 98.83°, which is smaller than the conventional angle of an ROO group due to the hydrogen-bond between H^3 and $O_{H_2O^1}$ bending the structure. H^1 was bound to the surface at 1.00 Å, forming hydrogen-bonds with the OOH group at 1.68 and 2.06 Å. H^2 and H^3 stayed in the same position on the surface as in I6. Charge analysis indicates that a charge of 1.52 e^- was transferred from the adsorbates to the surface (see Fig. 12). Compared to I6, an extra charge of 0.84 e^- migrated to the surface when the hydroperoxyl group was formed. The H^1, H^2, and H^4 atoms lost a total charge density of 1.74 e^-, which is consistent with the weakening of the OH bonds. $O_{H_2O^2}$ provided 0.38 e^- to form the OOH group, which led to the red shift of the stretching mode of the $O_{H_2O^2}H^3$ group and a weaker OH bond. $O_{H_2O^1}$ gained 0.21 e^- mostly from $O_{H_2O^1}$ and Cu_1, corresponding to the formation of the OOH group.

At stage I8, H^1 interacted with H^4, leading to the formation of a hydrogen molecule (see Fig. 10). The reaction energy ΔE_8 with respect to the previous step was calculated at 1.11 eV, showing that this step is endothermic, with a calculated activation energy E_{A6} of 1.13 eV. A stretching mode of 4225 cm^{-1} of the H^1H^4 bond, which is consistent with experimental data,[49] supports the formation of a hydrogen molecule (see Fig. 13). The stretching mode of the $O_{H_2O^1}O_{H_2O^2}$ bond was blue-shifted, as shown in Fig. 14, indicating a stronger OO bond compared to stage I7. Red shifts of the stretching modes of the OH^2 and OH^3 groups were observed, indicating that the OH bonds are weaker. The structure of I8 is shown in Fig. 11. The length of the H^1H^4 bond is 0.75 Å, which is in agreement with the bond length of a conventional hydrogen molecule.[48] The hydroperoxyl group was bent toward the surface, interacting via hydrogen-bonds with $O_{H_2O^1}$ and the surface at 1.89 and 1.88 Å, respectively. The H^2 atom located on top of the surface forms a short hydrogen-bond with $O_{H_2O^1}$ at 1.74 Å. The hydrogen molecule is 2.62 Å away from the surface, i.e., only weakly interacting with the system. Charge analysis indicates that the adsorbates lost 0.19 e^- to the surface (see Fig. 12). The H^2 atom lost 0.48 e^-, which is consistent with the red shift of the stretching mode and the weaker OH bond. A charge density of 0.28 e^- was transferred to $O_{H_2O^1}$ and $O_{H_2O^2}$, resulting in a stronger OO bond compared to the previous stage.

We further tested the desorption of the hydrogen molecule (see stage I9 in Fig. 10). The energy was calculated at 3.30 eV with respect to the reference system (pristine surface), which is a mere 0.09 eV higher than the previous step and therefore easily achievable. This result is consistent with the weak interaction of the hydrogen with the surface. Only negligible changes in the structure and energy of the system were observed.

The activation energies E_{A4} and E_{A5} for the formation of the hydroperoxide group and hydrogen were both greater than 2 eV, which is unlikely to be achievable under moderate conditions. However, the energy barrier for hydrogen generation was significantly reduced compared to pathways 1 and 2, as more charge density was transferred from the adsorbates to the surface, which weakened the OH bonds and increased the chemical reactivity of the surface. Our results suggest that pathway 3 represents a promising mechanism for hydrogen generation and desorption via photo- and/or electro-chemical water splitting.

C. Pathway on the reduced $CuWO_4$ (010) surface

Several studies have shown that the oxygen-vacancy-rich (010) surface of $CuWO_4$ can be used in photocatalytic and photoelectronic catalytic processes.[21–23] To investigate improvements in the catalytic performance of the $CuWO_4$ surface, we have investigated the reduced (010) surface by incorporating oxygen vacancies (O_v) and evaluated its activity toward water splitting and hydrogen evolution.

1. Reduced (010) surface

A single oxygen atom was removed from the pristine surface containing four formula units. Among the possible vacancy configurations, the most thermodynamically stable structure was obtained by removing the bridging oxygen atom between Cu and W atoms in the topmost layer. The resulting reduced surface slab was then doubled along the [001] and [100] directions to construct a larger supercell. The topmost layer then contained four oxygen vacancies per simulation cell, corresponding to a surface coverage of 0.5 ML. This coverage was selected based on the thermodynamic analysis of the $CuWO_4$ (010) surface under water-splitting conditions. In previous work, we tested both possible single-vacancy configurations and constructed a surface phase diagram to assess

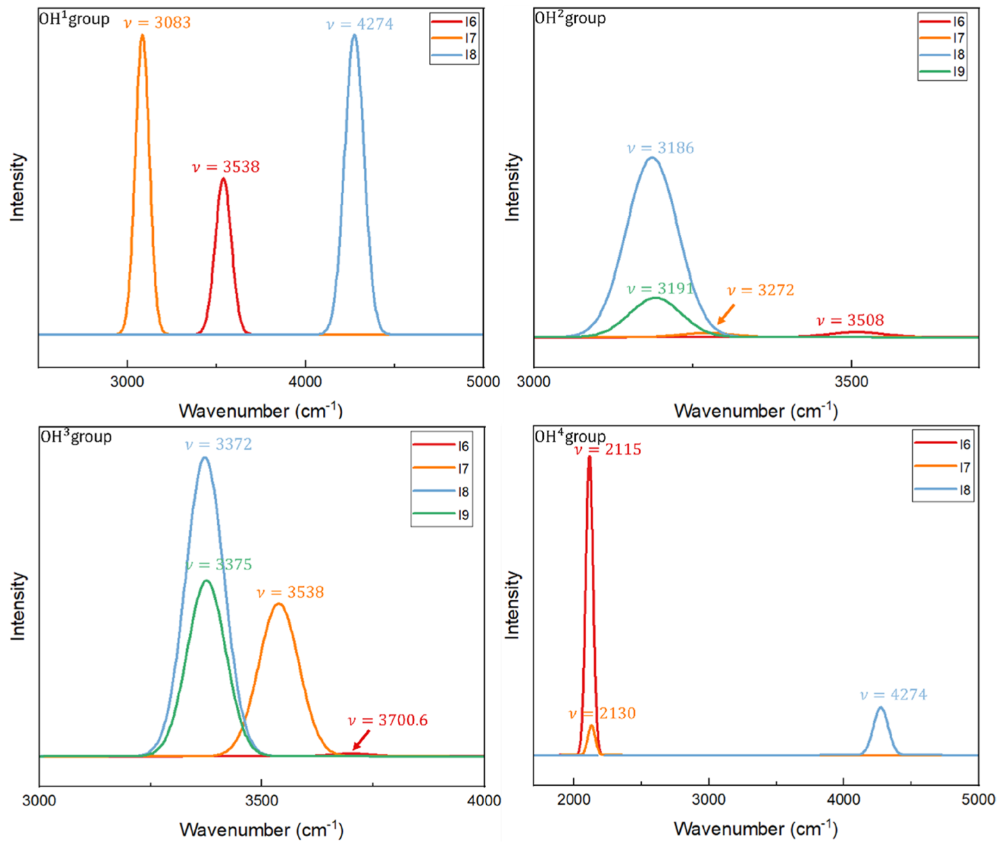

FIG. 13. Simulated IR spectra of the OH^1 (left top panel), OH^2 (right top panel), OH^3 (left bottom panel), and OH^4 (right bottom panel) groups on the (010) surface via pathway 3. The spectra of I6, I7, and I8 are colored in red, orange, and light blue, respectively, whereas the spectra of I9, I10, and I11 are colored in green, purple, and gold, respectively. υ is the stretching mode of the OH group for each intermediate, which is noted in the figure.

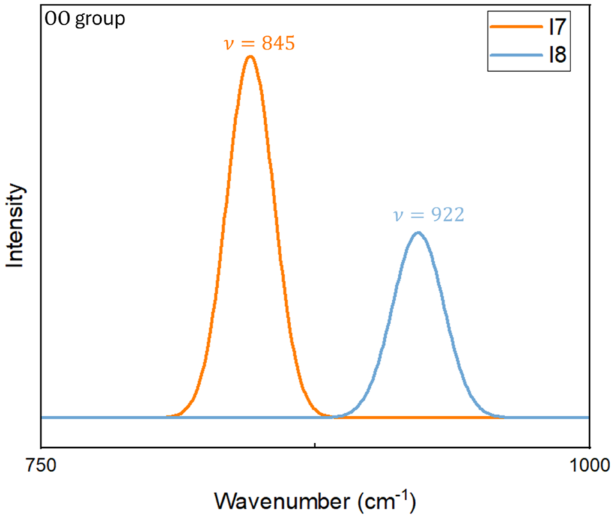

FIG. 14. Simulated IR spectra of the OO group on the (010) surface formed via pathway 3. Spectra I7 and I8 are colored in orange and light blue, respectively. υ is the stretching mode of the OH group of each intermediate, which is noted in the figure.

their relative stabilities at 298 K. The results showed that the surface is thermodynamically capable of losing one surface oxygen atom (per unit cell), corresponding to a 0.5 ML vacancy coverage under realistic reaction conditions.[25]

We acquired the scanning tunneling microscopy (STM) image of the reduced (010) surface at a distance (d) of 1.28 Å from the tip and a density of 0.05 e Å^{-3} [see Fig. 15(a)]. The Cu atoms and the O atoms in the sub-layer are shown as dark spots, whereas the coordinated O atoms on the top layer are represented by bright spots. The W atoms are shielded by the terminal O, which are therefore not observed in the STM image. The oxygen vacancies are represented by the dashed circles, which provide the potential adsorption sites for H_2O molecules. A negligible structural change was observed in the reduced surface with respect to the pristine (010) surface. The reduced surface is terminated by three-fold Cu and five-fold W atoms, whereas the O atoms stayed in the positions they occupied in the CuO_6 and WO_6 octahedral structures of the bulk phase [see Fig. 15(b)]. The distance between Cu and W adjacent to the oxygen vacancy of the reduced surface was 4.14 Å, as listed in Table II.

2. Pathway 4

At stage I1, a water molecule was introduced at the oxygen vacancy (O_{v_1}). Upon full structural relaxation, the water molecule

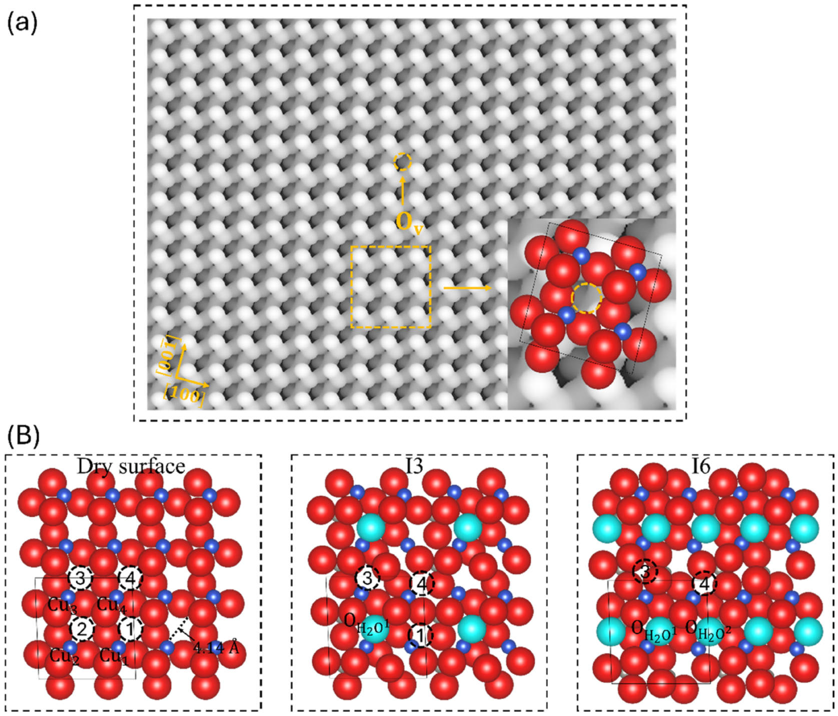

FIG. 15. (a) The topmost layer and the scanning tunneling microscopy (STM) image of the reduced (010) surface of $CuWO_4$. The Cu atoms and the O atoms in the sublayer are illustrated as the dark spots, whereas the coordinated O atoms on the top layer are represented as bright spots. (b) Top view of the reduced (010) surface and intermediates 3 and 6 of pathway 4. The Cu, W, and O atoms on the surface are in blue, gray, and red, respectively. The O of the water is in light blue. The oxygen vacancies 1–4 are represented as dashed circles. The distance between the Cu and W atoms adjacent to the oxygen vacancy of the dry surface is noted as a dashed line.

TABLE II. The distance between the Cu and W atom adjacent to the oxygen vacancy (d_{Cu-W}) and electron charge difference ($\Delta\rho$) of oxygen vacancies (O_v) of the dry surface, intermediate three (I3), and intermediate 6 (I6). $\Delta\rho_{CuO_3}$ and $\Delta\rho_{WO_3}$ represent the electron charge difference of the CuO_3 and WO_3 group adjacent to the oxygen vacancies.

Group	Properties	Dry surface	I3	I6
O_{v1}	d_{Cu-W}	4.14	3.82	3.34
	$\Delta\rho$	0	−0.27	−0.13
	$\Delta\rho_{CuO_3}$	0	−0.10	−0.07
	$\Delta\rho_{WO_5}$	0	−0.17	−0.06
O_{v2}	d_{Cu-W}	4.14	3.37	3.24
	$\Delta\rho$	0	−0.1	−0.15
	$\Delta\rho_{CuO_3}$	0	−0.06	−0.13
	$\Delta\rho_{WO_5}$	0	−0.04	−0.02
O_{v3}	d_{Cu-W}	4.14	3.54	3.15
	$\Delta\rho$	0	−0.12	−0.55
	$\Delta\rho_{CuO_3}$	0	−0.06	−0.53
	$\Delta\rho_{WO_5}$	0	−0.06	−0.02
O_{v4}	d_{Cu-W}	4.14	4.08	3.71
	$\Delta\rho$	0	−0.36	−0.27
	$\Delta\rho_{CuO_3}$	0	−0.22	−0.08
	$\Delta\rho_{WO_5}$	0	−0.14	−0.19

adsorbed dissociatively on the reduced $CuWO_4$ (010) surface with a large adsorption energy ΔE_1 of −2.39 eV with respect to the dry reduced surface, as shown in Fig. 16. $O_{H_2O^1}$ coordinated with Cu_2 and W_4, forming a bridging configuration with bond lengths of 1.98 and 2.11 Å, respectively (see Fig. 17). The dissociated proton H^2 bound a nearby surface oxygen at 1.03 Å, forming a hydrogen-bond with $O_{H_2O^1}$ at a distance of 1.49 Å. Charge density analysis revealed a net charge transfer of 0.12 e^- from the water molecule to the surface, primarily distributed along the O–W and O–H bonds, as illustrated in Fig. 18. Specifically, $O_{H_2O^1}$ gained 0.22 e^- mainly from W_4, H^2 lost 0.33 e^- to the surface, and the $O_{surface}$ bonded to H^2 acquired 0.18 e^-. To further understand the bonding environment, the vibrational frequencies for $O_{H_2O^1}H^1$ and $O_{surface}$ H^2 were calculated and compared to those of the isolated water molecule in the gas phase, as shown in Fig. 19. The stretching frequency of $O_{H_2O^1}H^1$ was estimated at 3703.4 cm^{-1}, showing a slight red shift relative to gas-phase H_2O, indicating a modest weakening of the O–H bond. In contrast, the $O_{H_2O^1}H^2$ bond exhibited a substantial red shift to 2481.5 cm^{-1}, suggesting a significantly weakened bond due to strong interaction with the surface. Compared to I2 in pathway 1, the reduced surface exhibited less charge transfer from the adsorbate due to the pre-existing electron density at the vacancy site, rendering the surface less electrophilic. The observed weakening of the OH^2 bond is attributed to stabilization by localized electrons at the oxygen vacancy, which redistributes charge and thereby reduces the bond strength.

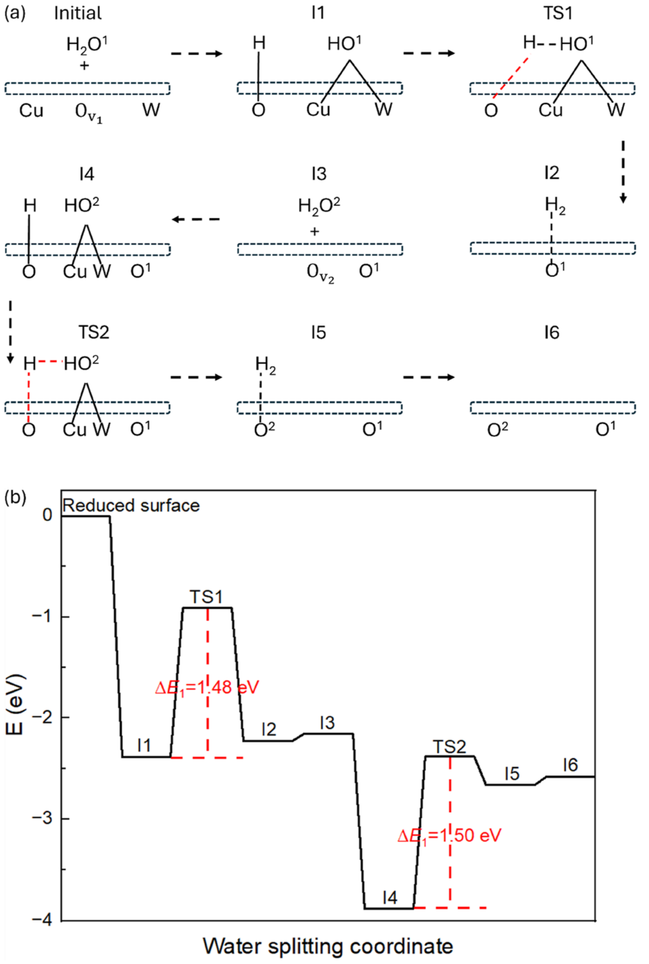

FIG. 16. (a) Proposed mechanism and (b) calculated reaction profile of pathway 4 on the reduced $CuWO_4$ (010) surface.

At stage I2, a H_2 molecule formed and was physisorbed on the surface with a reaction energy ΔE_2 of 0.16 eV and an activation energy ΔE_{A1} of 1.48 eV with respect to the previous step, as shown in Fig. 16. $O_{H_2O^1}$ remained at the oxygen vacancy site, bridging Cu_2 and W_4 in a configuration consistent with the previous step (see Fig. 17). However, the Cu_2-$O_{H_2O^1}$ and W_4-$O_{H_2O^1}$ bond lengths shortened to 1.87 and 1.77 Å, respectively. The hydrogen molecule, formed by the combination of H^1 and H^2, was weakly bound to the surface at a distance of 2.97 Å from $O_{H_2O^1}$, indicating minimal interaction with the surface. Charge density analysis revealed a net charge transfer of 0.90 e^- from the surface to $O_{H_2O^1}$, with Cu_2 and W_4 donating 0.13 e^- and 0.61 e^-, respectively (see Fig. 18). The result suggests that the $O_{H_2O^1}$ behaved as a lattice O, drawing charge from the adjacent Cu and W to stabilize its coordination environment. To confirm H_2 formation, we calculated the vibrational frequency of the H–H stretching mode, obtaining a value of 4291 cm^{-1} (see Fig. 19). The result is consistent with both the DFT-calculated and experimental values for gas-phase H_2,[51] which confirms successful H_2 evolution at the reduced surface.

At I3, the H_2 molecule desorbed from the surface with a ΔE_3 of 0.07 eV with respect to the previous step. The negligible energy difference compared to I2 further confirms the weak interaction between H_2 and the reduced surface. The structure and electronic configurations of I3 remained largely unchanged relative to I2. However, the distances between the Cu and W atoms adjacent to the oxygen vacancies shortened compared to the dry surface, as summarized in Table II and illustrated in Fig. 15. Specifically, the Cu–W distance (d_{Cu-W}) at O_{v2} decreased to 3.37 Å, likely due to the Coulombic attraction exerted by the bridging O atom from the dissociated water molecule $O_{H_2O^1}$. At O_{v1}, O_{v3}, and O_{v4}, the Cu–W distance was shortened to 3.82, 3.37, and 4.08 Å, respectively. We further analyzed the electron charge redistribution of atoms adjacent to the oxygen vacancies (Table II). Near O_{v1}, a total electron loss of 0.27 e^- was observed, primarily originating from the WO_5 group. The atoms neighboring O_{v2} exhibited a charge loss of 0.1 e^-, associated with bonding to the bridging $O_{H_2O^1}$. For O_{v3}, a charge migration of 0.12 e^- was observed, while the region around O_{v4} experienced a 0.36 e^- charge transfer, mainly contributed by CuO_3 (0.22 e^-) and WO_5 (0.14 e^-) groups. These results indicate that the adsorption of $O_{H_2O^1}$ at O_{v2} induced a redistribution of electron density, drawing charge from the surrounding vacancies toward the newly formed bridging Cu-$O_{H_2O^1}$-W. This, in turn, led to local lattice distortions and generated three inequivalent oxygen vacancy environments across the surface.

We further examined water adsorption at the remaining three oxygen vacancies, denoted as O_{v_2}, O_{v_3}, and O_{v_4}. Among them, dissociative adsorption at O_{v_2} was the most thermodynamically favorable configuration, with a calculated adsorption energy of −1.72 eV with respect to the previous step, as shown in I4 in Fig. 16. In this configuration, $O_{H_2O^2}$ occupied the O_{v_2} site and bridged between Cu_1 and W_3 at 2.54 and 2.01 Å, respectively (see Fig. 17). The dissociated proton bound to a neighboring surface oxygen with a bond length of 1.01 Å and formed a hydrogen bond with $O_{H_2O^2}$ at a distance of 1.64 Å. Charge analysis reveals a total charge transfer of 0.10 e^- from the adsorbed water molecule to the surface (see Fig. 18). Specifically, $O_{H_2O^2}$ gained 0.28 e^- upon occupying the vacancy site, primarily from W_3 (0.21 e^-). H^4 lost 0.33 e^- during the dissociation, of which 0.17 e^- was transferred directly to the surface. We further studied the vibrational frequencies of the OH groups, as illustrated in Fig. 19. The stretching mode of the $O_{H_2O^2}H^3$ group was slightly red-shifted to 3714 cm^{-1}, which is consistent with a modest charge transfer of 0.05 e^- from H^3 to $O_{H_2O^2}$. In contrast, the stretching mode of $O_{surface}H^4$ exhibited a pronounced red shift to 2893 cm^{-1} with respect to the isolated water molecule in the gas phase, indicating a significant weakening of the OH bond due to interaction with the surface.

At stage I5, the second hydrogen molecule was formed from H^3 and H^4 with a ΔE_5 of 1.22 eV and an activation energy of 1.50 eV with respect to the previous step (see Fig. 16). $O_{H_2O^2}$ bridged Cu_1 and W_3 with bond distances of 2.11 and 1.76 Å, respectively, as shown in Fig. 17. The hydrogen molecule was physisorbed on the surface at 2.56 Å. Charge analysis indicates that a total amount charge of 0.90 e^- migrated from the surface to adsorbate (see Fig. 18). $O_{H_2O^2}$ gained 0.88 e^-, mostly contributed by W_3 (0.55 e^-). Additionally, Cu_3 lost 0.21 e^- during the process of hydrogen formation, with

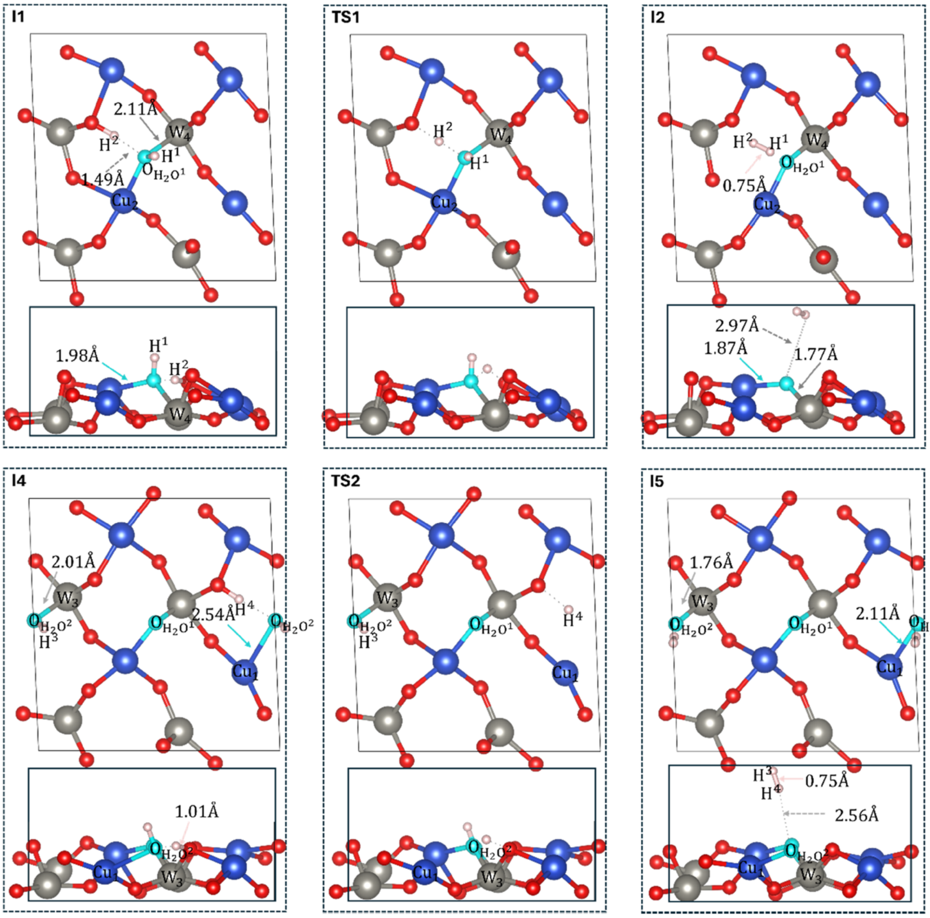

FIG. 17. Top and side view of the structures of the intermediates and transition states along pathway 4 on the reduced $CuWO_4$ (010) surface. The Cu, W, and O atoms on the surface are in blue, gray, and red, respectively. The O and H atoms of water are in light blue and white, respectively, and hydrogen-bonds are shown as dotted lines.

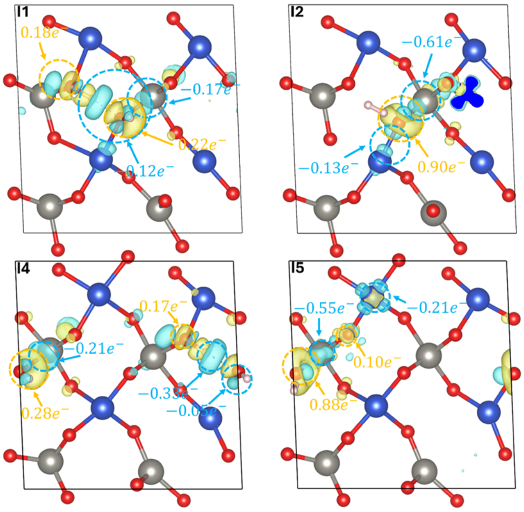

FIG. 18. Charge density difference plots for the different stages along the water splitting process via pathway 4 on the reduced $CuWO_4$ (010) surface. Blue regions represent charge gain, whereas yellow regions represent charge depletion.

0.1 e^- transferring to the bridging O with W_3. The stretch mode of H^3–H^4 was estimated at 4278 cm^{-1}, as shown in Fig. 19. The result is consistent with experiment,[51] supporting the formation of a hydrogen molecule.

At stage I6, the second hydrogen molecule desorbed from the surface with a ΔE_6 of 0.08 eV with respect to the previous step. This value is hardly different from I5, indicating a weak interaction between molecular hydrogen and the surface. The overall structural and electronic properties at I6 remained largely unchanged relative to I5. However, compared to the dry surface and I3, the top layer exhibited further structural distortion, following the adsorption of the newly formed bridging $O_{H_2O^2}$ (see Fig. 15). Specifically, the Cu–W distances contracted to 3.34 and 3.24 Å for O_{v1} and O_{v2}, driven by the Coulombic attraction exerted by the bridging O atom (Table II). At O_{v3} and O_{v4}, the Cu–W distance decreased markedly to 3.15 and 3.71 Å, respectively. Additional calculations confirmed that water molecules were no longer able to adsorb at O_{v3} and O_{v4} under these conditions. We further analyzed the electron charge redistribution across the surface, as detailed in Table II. Near O_{v3}, a total charge loss of 0.55 e^- was observed, predominantly contributed by the CuO_3 group (0.53 e^-). The region surrounding O_{v4} exhibited a charged migration of 0.27 e^-, mainly originating

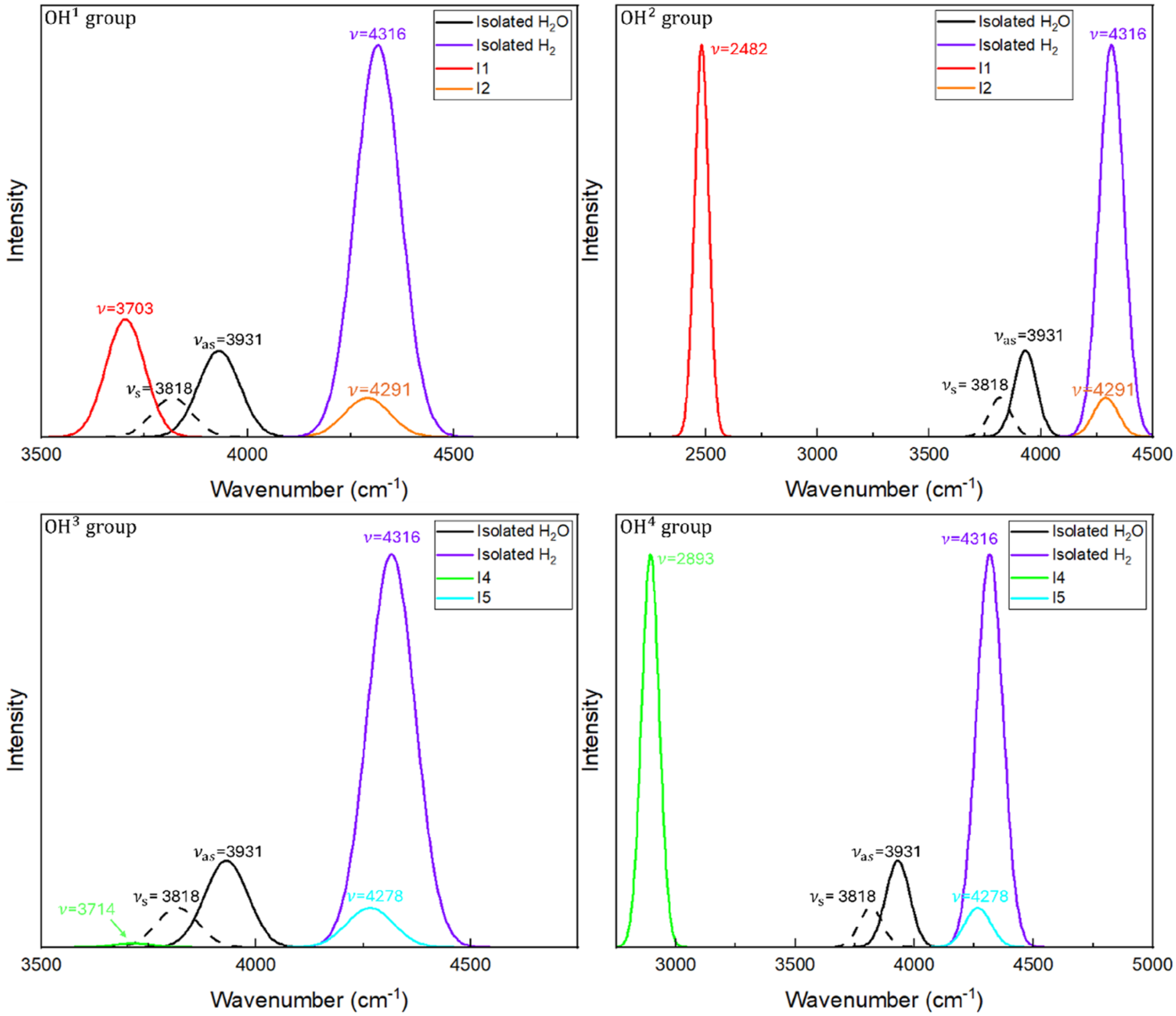

FIG. 19. Simulated IR spectra of the OH^1 (left top panel), OH^2 (right top panel), OH^3 (left bottom panel), and OH^4 (right bottom panel) groups on the reduced (010) surface via pathway 4. The spectra of I1, I2, I3, and I4 are colored in red, orange, green, and light blue, respectively. υ is the stretching mode of the OH group for each intermediate, which are noted in the figure. υ_{as} and υ_s represent the asymmetrical and symmetrical stretching modes of molecular water, respectively.

from the WO_5 group (0.23 e^-). These findings show that the formation of bridging Cu-O_{H_2O}-W draws electron density from neighboring oxygen vacancies, inducing local lattice distortions and reducing the availability of reactive sites, ultimately hindering further water adsorption.

Compared with pathways 1 and 2, the presence of an oxygen vacancy plays a critical role in the catalytic efficacy. The removal of a lattice oxygen creates under-coordinated metal sites and introduces localized excess electrons, making the surface more electron-rich and chemically active. These changes enhance the adsorption and stabilization of hydrogen intermediates and lower the energy of the transition state for H_2 formation. However, the reduced surface would need to be re-created after the reaction.

While the present study has focused on isolated oxygen vacancies and their effect on water adsorption and dissociation, it is important to consider the potential for surface reconstruction under more aggressive reduction conditions. Dual-metal active sites have been reported in other catalytic systems to enhance activity through electronic synergy and cooperative adsorbate binding.[53,54] However, in our relaxed reduced $CuWO_4$ (010) surface model, no such dual-center configuration formed spontaneously. The Cu and W atoms adjacent to the vacancy remained over 4.0 Å apart, and adsorbed water preferentially interacted with the Cu site. These findings suggest that the intrinsic lattice structure imposes constraints on metal–metal pairing. Further exploration of defect clustering, doping, or thermally activated reconstructions may reveal new opportunities for creating such synergistic catalytic motifs on $CuWO_4$ surfaces.

IV. CONCLUSION

We have employed DFT+U-D3 calculations to investigate the thermally activated surface reactions of water adsorption, splitting, and hydrogen generation over the pristine and reduced $CuWO_4$ (010) surface. Four potential reaction pathways were analyzed, including the thermodynamic and kinetic profiles, intermediates, and transition states. For the pristine (010) surface, among the pathways studied, pathway 3 via a hydroperoxide group stands out as a promising mechanism, owing to its significant charge density migration from adsorbates to the surface, which weakens the OH bonds and enhances surface reactivity. This pathway facilitates the formation and desorption of hydrogen with reduced energy barriers compared to pathways 1 and 2. However, the formation of the hydroperoxide group and hydrogen molecule still requires activation energies exceeding 2 eV, indicating that additional strategies, such as co-catalysts, surface modifications, or additional energy sources, may be necessary to optimize the reaction under conventional catalytic conditions.

In pathway 4, applied at the reduced (010) surface, the presence of an oxygen vacancy on the $CuWO_4$ (010) surface significantly enhances the hydrogen evolution reaction by modifying both the electronic and structural properties of the active site. The vacancy introduces under-coordinated Cu and W atoms and localized excess electrons, which together increase the surface chemical reactivity, as well as providing an attractive adsorption site for the oxygen of the water molecule. These changes stabilize hydrogen-containing intermediates through stronger adsorption and promote charge redistribution that weakens O–H bonds. The charge rearrangement lowers the activation barrier for H–H combination and facilitates the formation and subsequent desorption of molecular hydrogen. However, the reduced surface is typically synthesized under N_2 or noble gas-rich atmospheres,[50,51] which may limit its direct applicability under conventional water-splitting conditions.

We consider that our findings provide valuable insights into the potential photo-electrochemical water splitting mechanism over $CuWO_4$, offering a foundation for future research aimed at enhancing the efficiency of hydrogen production for sustainable energy applications. In view of the superior performance of the reduced (010) surface, future work will include the introduction of dopants in the surface, for example, cations of lower valence than tungsten, to facilitate the formation of stable oxygen vacancies in the surface, which may aid the catalytic formation of hydrogen.

ACKNOWLEDGMENTS

X.C. is grateful to the UK Engineering & Physical Sciences Research Council and the University of Leeds for the provision of a Research Scholarship. We thank Dr. David Santos-Carballal and Dr. Marietjie Ungerer for useful discussions. Via our membership of the UK's HEC Materials Chemistry Consortium, which is funded by EPSRC (Grant No. EP/X035859), this work made use of the ARCHER2 UK National Supercomputing Service (https://www.archer2.ac.uk). This research has also used ARC4, part of the High-Performance Computing facilities at the University of Leeds, UK. All data are provided in full in the Results and Discussion section of this paper. For the purpose of Open Access, the authors have applied a CC BY public copyright license to any Author Accepted Manuscript version arising from this submission.

AUTHOR DECLARATIONS

Conflict of Interest

The authors have no conflicts to disclose.

Author Contributions

Xuan Chu: Conceptualization (equal); Data curation (equal); Formal analysis (equal); Investigation (equal); Methodology (equal); Writing – original draft (equal); Writing – review & editing (equal). **Nora H de Leeuw**: Conceptualization (equal); Data curation (equal); Formal analysis (equal); Funding acquisition (equal); Investigation (equal); Methodology (equal); Project administration (equal); Resources (equal); Software (equal); Supervision (equal); Validation (equal); Writing – review & editing (equal).

DATA AVAILABILITY

The data that support the findings of this study are available from the corresponding author upon reasonable request.

REFERENCES

[1] L. Yang, F. Li, and Q. Xiang, "Advances and challenges in the modification of photoelectrode materials for photoelectrocatalytic water splitting," Mater. Horiz. **11**, 1638–1657 (2024).

[2] T. Yao, X. An, H. Han, J. Q. Chen, and C. Li, "Photoelectrocatalytic materials for solar water splitting," Adv. Energy Mater. **8**, 1800210 (2018).

[3] K. Maeda, "Photocatalytic water splitting using semiconductor particles: History and recent developments," J. Photochem. Photobiol., C **12**, 237–268 (2011).

[4] J. Abdul Nasir, A. Munir, N. Ahmad, T. u. Haq, Z. Khan, and Z. Rehman, "Photocatalytic Z-Scheme overall water splitting: Recent advances in theory and experiments," Adv. Mater. **33**, 2105195 (2021).

[5] O. F. Aldosari, "Photocatalytic water-splitting for hydrogen production using TiO_2-based catalysts: Advances, current challenges, and future perspectives," Catal. Rev. 1–38 (2025).

[6] S. Nishioka, F. E. Osterloh, X. Wang, T. E. Mallouk, and K. Maeda, "Photocatalytic water splitting," Nat. Rev. Methods Primers **3**, 42 (2023).

[7] K. Zhang and R. Zou, "Advanced transition metal-based OER electrocatalysts: Current status, opportunities, and challenges," Small **17**, 2100129 (2021).

[8] D.-D. Qin, Y. Tang, G. Ma, L. Qin, C.-L. Tao, X. Zhang, and Z. Tang, "Molecular metal nanoclusters for ORR, HER and OER: Achievements, opportunities and challenges," Int. J. Hydrogen Energy **46**, 25771–25781 (2021).

[9] S. Chen, T. Takata, and K. Domen, "Particulate photocatalysts for overall water splitting," Nat Rev Mater **2**, 17050 (2017).

[10] B. You and Y. Sun, "Innovative strategies for electrocatalytic water splitting," Acc. Chem. Res. **51**, 1571–1580 (2018).

[11] S. Y. Tee, K. Y. Win, W. S. Teo, L. Koh, S. Liu, C. P. Teng, and M. Han, "Recent progress in energy-driven water splitting," Adv. Sci. **4**, 1600337 (2017).

[12] T. Hisatomi, J. Kubota, and K. Domen, "Recent advances in semiconductors for photocatalytic and photoelectrochemical water splitting," Chem. Soc. Rev. **43**, 7520–7535 (2014).

[13] P. Raizada, S. Sharma, A. Kumar, P. Singh, A. A. Parwaz Khan, and A. M. Asiri, "Performance improvement strategies of $CuWO_4$ photocatalyst for hydrogen generation and pollutant degradation," J. Environ. Chem. Eng. **8**, 104230 (2020).

[14] C. R. Lhermitte and B. M. Bartlett, "Advancing the chemistry of $CuWO_4$ for photoelectrochemical water oxidation," Acc. Chem. Res. **49**, 1121–1129 (2016).

[15] J. U. Lee, J. H. Kim, and J. S. Lee, "Emergent CuWO4 photoanodes for solar fuel production: Recent progress and perspectives," Catalysts **13**, 1408 (2023).

[16] Y.-L. Tang, N. Rong, F. L. Liu *et al.*, "Enhancement of the photoelectrochemical performance of $CuWO_4$ films for water splitting by hydrogen treatment," Appl. Surf. Sci. **361**, 133–140 (2016).

[17] J. Ke, M. Adnan Younis, Y. Kong, H. Zhou, J. Liu, L. Lei, and Y. Hou, "Nanostructured ternary metal tungstate-based photocatalysts for environmental purification and solar water splitting: A review," Nanomicro Lett **10**, 69 (2018).

[18] S. Wang and L. Wang, "Recent progress of tungsten- and molybdenum-based semiconductor materials for solar-hydrogen production," Tungsten **1**, 19–45 (2019).

[19] X. Bai, Z. Fu, X. Ma, Z. Zhang, J. Fan, E. Liu, and J. Li, "Hydrophilic regulated photocatalytic converting phenol selectively over S-scheme $CuWO_4/TiO_2$," J. Cleaner Prod. **369**, 133099 (2022).

[20] P. Sharma, A. Kumar, G. Sharma, T. Wang, P. Dhiman, and F. J. Stadler, "Recent advances in oxygen vacancies rich Z-scheme and S-scheme heterojunctions for water treatment and hydrogen production," Inorg. Chem. Commun. **161**, 112112 (2024).

[21] D. Xiang, X. Jin, G. Sun, C. Zhong, and S. Gao, "Oxygen vacancy engineering of ultra-small $CuWO_4$ nanoparticles for boosting photocatalytic organic pollutant degradation," Dalton Trans. **53**, 7839 (2024).

[22] W. Guo, Y. Wang, X. Lian, Y. Nie, S. Tian, S. Wang, Y. Zhou, and G. Henkelman, "Insights into the multiple effects of oxygen vacancies on $CuWO_4$ for photoelectrochemical water oxidation," Catal. Sci. Technol. **10**, 7344 (2020).

[23] W. Chen, W.-J. Zhang, K. Wang *et al.*, "Oxygen vacancy-mediated $CuWO_4/CuBi_2O_4$ samples with efficient charge transfer for enhanced catalytic activity toward photodegradation of pharmacologically active compounds," Langmuir **39**(49), 17830–17843 (2023).

[24] X. Chu, D. Santos-Carballal, and N. H. de Leeuw, "Water adsorption at the (010) and (101) surfaces of $CuWO_4$," Phys. Chem. Chem. Phys. **26**, 28628–28642 (2024).

[25] X. Chu, D. Santos-Carballal, and N. H. de Leeuw, "Exploring the redox properties of the Low–Miller index surfaces of copper tungstate ($CuWO_4$): Evaluating the impact of the environmental conditions on the water splitting and carbon dioxide reduction processes," J. Phys. Chem. C **127**, 18944–18961 (2023).

[26] G. Kresse and J. Hafner, "*Ab initio* molecular dynamics for liquid metals," Phys. Rev. B **47**, 558–561 (1993).

[27] G. Kresse and J. Hafner, "*Ab initio* molecular-dynamics simulation of the liquid-metal–amorphous-semiconductor transition in germanium," Phys. Rev. B **49**, 14251–14269 (1994).

[28] J. P. Perdew, K. Burke, and M. Ernzerhof, "Generalized gradient approximation made simple," Phys. Rev. Lett. **77**, 3865–3868 (1996).

[29] G. Kresse and J. Furthmüller, "Efficient iterative schemes for *ab initio* total-energy calculations using a plane-wave basis set," Phys. Rev. B **54**, 11169–11186 (1996).

[30] S. Grimme, "Semiempirical GGA-type density functional constructed with a long-range dispersion correction," J. Comput. Chem. **27**, 1787–1799 (2006).

[31] T. Suter, E. G. Webb, H. R. C. BöhniAlkire, and R. C. Alkire, "Pit initiation on stainless steels in 1 M NaCl with and without mechanical stress," J. Electrochem. Soc. **148**, B174 (2001).

[32] L. Schimka, J. Harl, and G. Kresse, "Improved hybrid functional for solids: The HSEsol functional," J. Chem. Phys. **134**, 024116 (2011).

[33] J. Jaramillo, G. E. Scuseria, and M. Ernzerhof, "Local hybrid functionals," J. Chem. Phys. **118**, 1068–1073 (2003).

[34] D. J. Chadi, "Special points for Brillouin-zone integrations," Phys. Rev. B **16**, 1746–1747 (1977).

[35] D. Sheppard, R. Terrell, and G. Henkelman, "Optimization methods for finding minimum energy paths," J. Chem. Phys. **128**, 134106 (2008).

[36] P. E. Blöchl, O. Jepsen, and O. K. Andersen, "Improved tetrahedron method for Brillouin-zone integrations," Phys. Rev. B **49**, 16223–16233 (1994).

[37] M. Barma, "Gaussian smearing of spin weight functions in models of phase transitions," J. Phys. A Math. Gen. **16**, L745–L750 (1983).

[38] G. Henkelman and H. Jónsson, "Improved tangent estimate in the nudged elastic band method for finding minimum energy paths and saddle points," J. Chem. Phys. **113**, 9978–9985 (2000).

[39] G. Henkelman, B. P. Uberuaga, and H. Jónsson, "A climbing image nudged elastic band method for finding saddle points and minimum energy paths," J. Chem. Phys. **113**, 9901–9904 (2000).

[40] G. Henkelman, A. Arnaldsson, and H. Jónsson, "A fast and robust algorithm for Bader decomposition of charge density," Comput. Mater. Sci. **36**, 354–360 (2006).

[41] W. Tang, E. Sanville, and G. Henkelman, "A grid-based Bader analysis algorithm without lattice bias," J. Phys.: Condens. Matter **21**, 084204 (2009).

[42] P. W. Tasker, "The stability of ionic crystal surfaces," J. Phys. C: Solid State Phys. **12**, 4977–4984 (1979).

[43] G. W. Watson, E. T. Kelsey, N. H. de Leeuw, D. J. Harris, and S. C. Parker, "Atomistic simulation of dislocations, surfaces and interfaces in MgO," J. Chem. Soc., Faraday Trans. **92**, 433 (1996).

[44] M. W. Wong, "Vibrational frequency prediction using density functional theory," Chem. Phys. Lett. **256**, 391–399 (1996).

[45] A. P. Scott and L. Radom, "Harmonic vibrational frequencies: An evaluation of Hartree–Fock, Møller–Plesset, quadratic configuration interaction, density functional theory, and semiempirical Scale factors," J. Phys. Chem. **100**, 16502–16513 (1996).

[46] M. D. Halls, J. Velkovski, and H. B. Schlegel, "Harmonic frequency scaling factors for Hartree–Fock, S-VWN, B-LYP, B3-LYP, B3-PW91 and MP2 with the Sadlej pVTZ electric property basis set," Theor. Chem. Acc. **105**, 413–421 (2001).

[47] D. Santos-Carballal, A. Roldan, and N. H. de Leeuw, "Early oxidation processes on the greigite Fe_3S_4 (001) surface by water: A density functional theory study," J. Phys. Chem. C **120**, 8616–8629 (2016).

[48] D. B. Lawson and J. F. Harrison, "Distance dependence and spatial distribution of the molecular quadrupole moments of H_2, N_2, O_2, and F_2," J. Phys. Chem. A **101**(26), 4781–4792 (1997).

[49] G. D. Dickenson, M. L. Niu, E. J. Salumbides *et al.*, "Fundamental vibration of molecular hydrogen," Phys. Rev. Lett. **110**, 193601 (2013).

[50] D. E. P. Vanpoucke and G. Brocks, "Formation of Pt-induced Ge atomic nanowires on Pt/Ge(001): A density functional theory study," Phys. Rev. B **77**, 241308 (2008).

[51] A. R. Hoy and P. R. Bunker, "A precise solution of the rotation bending Schrodinger equation for a triatomic molecule with application to the water molecule," J. Mol. Spectrosc. **74**, 1–8 (1979).

[52] D. Friebel, M. W. Louie, M. Bajdich *et al.*, "Identification of highly active Fe sites in (Ni,Fe)OOH for electrocatalytic water splitting," J. Am. Chem. Soc. **137**(3), 1305–1313 (2015).

[53] N. Wang, E. Li, Z. Lyu *et al.*, "Single/dual-atom electrocatalysts for water splitting related reaction at neutral pH," Next Nanotechn. **6**, 100073 (2024).

[54] A. Kumar, V. Q. Bui, J. Lee *et al.*, "Moving beyond bimetallic-alloy to single-atom dimer atomic-interface for all-pH hydrogen evolution," Nat. Commun. **12**, 6766 (2021).